AFRRI Reports

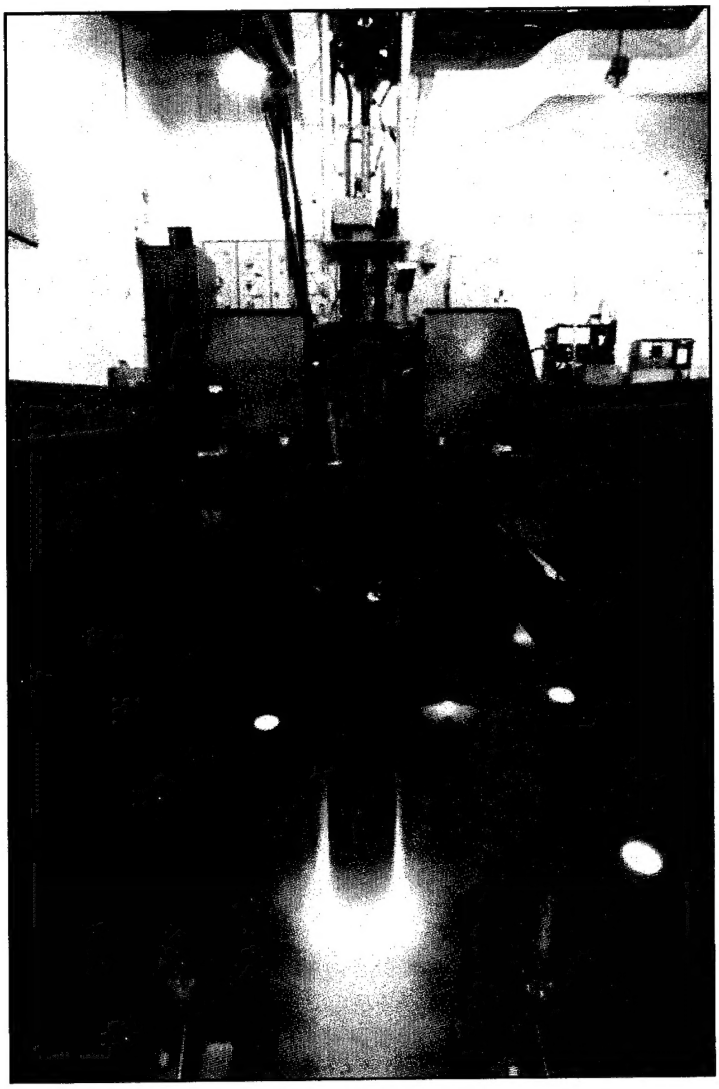

Third Quarter
1995

Armed Forces Radiobiology Research Institute
8901 Wisconsin Avenue
Bethesda, Maryland 20889-5603

On the cover: The glow in the pool of water shielding the core of AFRRI's Mark-F TRIGA nuclear reactor is known as Cherenkov radiation and is caused by electrons from the reactor traveling at speeds greater than the speed of light in water. The effect is named for Pavel Alekseyevich Cherenkov, a Soviet scientist who, along with his co-investigators, won the 1958 Nobel Prize for Physics for their observations.
AFRRI photo by David H. Morse.

REPORT DOCUMENTATION PAGE

Form Approved
OMB No. 0704-0188

1. AGENCY USE ONLY *(Leave blank)*	2. REPORT DATE	3. REPORT TYPE AND DATES COVERED
	November 1995	Reprints

4. TITLE AND SUBTITLE

AFRRI Reports, Third Quarter 1995

5. FUNDING NUMBERS

PE: NWED QAXM

6. AUTHOR(S)

7. PERFORMING ORGANIZATION NAME(S) AND ADDRESS(ES)

Armed Forces Radiobiology Research Institute
8901 Wisconsin Avenue
Bethesda, MD 20889-5603

8. PERFORMING ORGANIZATION REPORT NUMBER

SR95-17 - SR95-21

9. SPONSORING/MONITORING AGENCY NAME(S) AND ADDRESS(ES)

Uniformed Services University of the Health Sciences
4301 Jones Bridge Road
Bethesda, MD 20814-4799

10. SPONSORING/MONITORING AGENCY REPORT NUMBER

11. SUPPLEMENTARY NOTES

12a. DISTRIBUTION/AVAILABILITY STATEMENT

Approved for public release; distribution unlimited.

12b. DISTRIBUTION CODE

13. ABSTRACT *(Maximum 200 words)*

This volume contains AFRRI Scientific Reports SR95-17 through SR95-21 for July-September 1995.

14. SUBJECT TERMS

15. NUMBER OF PAGES
53

16. PRICE CODE

17. SECURITY CLASSIFICATION OF REPORT	18. SECURITY CLASSIFICATION OF THIS PAGE	19. SECURITY CLASSIFICATION OF ABSTRACT	20. LIMITATION OF ABSTRACT
UNCLASSIFIED	UNCLASSIFIED	UNCLASSIFIED	UL

CLASSIFIED BY:

DECLASSIFY ON:

CONTENTS

Application of the Premature Chromosome Condensation Assay in Simulated Partial-Body Radiation Exposures: Evaluation of the Use of an Automated Metaphase-Finder

W. F. Blakely,[a] *P. G. S. Prasanna*,[a] *C. J. Kolanko*,[a] *M. D. Pyle*,[a] *D. M. Mosbrook*,[a] *A. S. Loats*,[b] *T. L. Rippeon*,[b] *H. Loats*[b]

[a]Armed Forces Radiobiology Research Institute, Radiation Biophysics Department, Bethesda, Maryland, USA; [b]Loats Associates, Westminster, Maryland, USA

Key Words. Premature chromosome condensation assay • Lymphocytes • x-ray • Chromosome damage • Biodosimetry • Partial-body exposure • Metaphase-finder

Abstract. The premature chromosome condensation (PCC) assay has been proposed as a useful and rapid end point for biological dosimetry following accidental high-dose radiation overexposures. A major benefit of the PCC assay is that it does not require cells to divide for evaluation of cytogenetic damage. The PCC assay was performed on isolated human peripheral lymphocytes exposed in vitro to doses from 1 to 9 Gy of 250 kVp x-rays. The dose-response relationships of the frequency distribution and the yield of PCC fragments in cells were determined after one day of repair at 37°C. A Q_{pcc} approach, which involves the analysis of the yield of excess PCC fragments in damaged cells, was used to establish a dose-response calibration curve. This method is identical in concept to the Q_{dr} technique introduced by *Sasaki* [1] for partial-body exposure dose-estimates using asymmetrical chromosome aberrations (i.e., dicentrics and rings) in metaphase spreads of human lymphocytes. A simulated in vitro test of a partial-body exposure to a 6-Gy dose was performed. The results from this test provided dose estimates of 5.3 ± 0.6, 4.7 ± 0.6, 5.0 ± 0.6 and 4.7 ± 0.8 Gy for the 20, 30, 50 and 75 percent component of 6-Gy irradiated cells, respectively. An automated metaphase-finding system was evaluated for use with the PCC assay. This system helped to locate PCC spreads among the mitotic inducer Chinese hamster ovary (CHO) metaphase spreads, thereby facilitating rapid scoring of samples. We conclude that the measurement of excess PCC fragments in Giemsa-stained preparations provides useful biological dosimetry information on the size of the irradiated fraction in cases of acute radiation exposures. Use of Q_{pcc} analysis is recommended for partial-body exposures to determine dose estimates for the irradiated fraction. Automated metaphase finding significantly enhances the speed of the PCC assay.

Correspondence: Dr. William F. Blakely, Armed Forces Radiobiology Research Institute, Radiation Biophysics Department, 8901 Wisconsin Avenue, Bethesda, MD 20889-5603, USA.

Received October 19, 1994; accepted for publication October 19, 1994. 1066-5099/95/$5.00/0

Introduction

The premature chromosome condensation (PCC) technique, initially introduced by *Johnson* and *Rao* [2], involves either ultraviolet light-inactivated Sendai virus [2, 3] or polyethylene glycol (PEG) [3, 4] assisted fusion of mitotic "inducer" cells with "test" interphase cells. A mitotic factor from the mitotic inducer cells is believed to cause a dissolution of the nuclear envelope and subsequent premature condensation of interphase DNA. In the case of a nonirradiated and resting G_1 human lymphocyte, this process permits visualization of 46 single-chromatid-like structures, which appear along with the conventional metaphase chromosomes of the mitotic inducer cell following appropriate hypotonic swelling, fixation and staining.

Ionizing radiation causes an increase in the number of PCC fragments in cells. The PCC assay has been used to examine the effects of radiation quality and the kinetics of repair following exposure of mammalian cells to low- and high-linear energy transfer (LET) radiations [5-9]. *Bedford* and *Goodhead* [10] showed that alpha particles (3.2 MeV, 128 keV/μm)

produced a relative biological effectiveness (RBE) of 2.2 for the early production of excess PCC fragments in noncycling HF19 human diploid fibroblasts. *Pantelias* and *Maillie* [11] demonstrated that even though rat peripheral blood lymphocytes have undergone significant repair by one day following whole-body exposure to 3 Gy x-rays, elevated yields of excess PCC fragments can still be detected for several days postirradiation.

The PCC assay has been suggested as a valuable end point for use as a biological indicator for radiation doses in cases of accidental radiation exposures [4, 12]. Since the PCC technique does not require the stimulation of resting cells to proliferate, radiation injury in cells that otherwise would not proceed into mitosis can be visualized. A significant advantage of the PCC technique is that it is rapid and affords the opportunity for cytogenetic laboratories to provide results within one day of receipt of a peripheral blood sample.

Dose inhomogeneity is a major factor to consider in biodosimetry studies. Relying primarily upon the use of the measurement of dicentrics and rings in metaphase spreads from stimulated human lymphocytes, dose inhomogeneity has been addressed by several approaches, including the contaminated Poisson [13, 14] and Q_{dr} [1, 13] methods. *Natarajan* and colleagues recently demonstrated that the PCC assay, compared with the dicentric and micronuclei assay, provides a more accurate prediction of small fractions of partial-body exposures [15].

Searching for metaphases represents the major time-consuming and tedious part for a cytogenetic laboratory that scores chromosome aberrations [16]. The use of an automated metaphase-finding system offers significant benefit in the study of rogue cells [17], in the survey of populations of occupationally irradiated workers, and in cases of dose estimations for radiation accidents involving partial-body exposures [16]. Reduction in labor costs associated with the scoring of large number of samples represents the major benefit. At present, it is not known whether any of the commercially available metaphase-finders would require adaption for use in the PCC assay, where PCC spreads represent a small fraction (<10%) of the mitotic inducer cell spreads.

We evaluated the application of the PCC assay for estimation of the irradiation fraction and dose to the irradiated fraction in simulated partial-body exposures as well as the feasibility of using an automated metaphase-finding system to expedite locating PCC spreads for analysis.

Materials and Methods

Mitotic Cells

Mitotic Chinese hamster ovary (CHO) cells, which were used as mitotic-inducer cells in the PCC assay, were obtained by a modified mitotic-cell collection protocol suggested by *E. A. Blakely* of Lawrence Berkeley Laboratory, CA. This protocol is based on colchicine-induced inhibition of cell progression in metaphase, followed by repeated sequential mitotic "shake-off" procedures of the colchicine-treated CHO cells.

CHO cells were maintained as stock cultures in complete growth media consisting of α-minimum essential medium (α-MEM) supplemented with fetal bovine serum, sodium bicarbonate and antibiotics; cells were grown at 37°C in an atmosphere of 5% CO_2/95% air with biweekly subculturing. In the mitotic collection experiments, exponentially growing cells were plated into tissue-culture flasks so that after one day the flask was subconfluent. Typically, several preshakes were performed to dislodge dead, loosely-attached or floating cells. Mitotic cells were then harvested from a total of three 3.5 h collection intervals with complete medium containing 2 μg/ml of colchicine (mitotic medium), pelleted by centrifugation (4°C), and resuspended in mitotic medium (4°C); then a cell count was performed. Typically, the mitotic index of this cell suspension ranged from 0.93 to 0.97, based on microscopic examination of more than 1,000 Geisma-stained cells in smears. Approximately 1×10^6 mitotic cells were then transferred to cyrovials (Nunc Cryotubes, Intermed, Roskilde, Denmark) in mitotic medium containing 10% dimethyl sulfoxide. Cells in cryovials were then placed in a freezing container (Cryo 1°C freezing container, Cat. No. 5100-0001, Nalgene Corp., Rochester, NY) that was transferred to a mechanical freezer (–70°C) for a controlled-rate freezing (i.e., –1°C/min). After 24 h the cryovials were transferred to a liquid-nitrogen storage container until later use in the PCC-assay.

Lymphocyte Culture

Whole blood from healthy human donors was collected into standard blood collection

tubes containing ethylenediamine tetraacetate acid (EDTA) (Becton-Dickinson, Rutherford, NJ). The informed consent form used in this study was approved by the Uniformed Services University of the Health Sciences, Human Use Committee, Bethesda, MD. Lymphocytes were isolated from whole peripheral blood using Ficoll (Histopaque 1077, Sigma Chemical Co., St. Louis, MO) gradients, washed with phosphate buffered saline (PBS), and suspended in complete growth medium (KaryoMax Bone Marrow Karyotyping Medium, GIBCO BRL, Gaithersburg, MD). Cell cultures were typically aerated in complete culture media in tissue-culture flasks for at least 30 min at 37°C prior to either sham treatment or exposure to radiation.

Irradiation Procedure and Dosimetry

Cells suspended in culture media in tissue-culture flasks were irradiated on a rotating Plexiglas holder with a Phillips industrial x-ray machine (Phillips GMBH, Hamburg, Germany) at room temperature. The irradiation conditions were a dose rate of 1 Gy/min with an effective energy of 83 keV (source-to-surface distance was approximately 55 cm, 250 kVp at 12.5 mA, filtration with 0.20 mm Cu and 1.0 mm Al) [18]. Dosimetry was determined using ion chambers placed in tissue-culture flasks filled with tissue-equivalent plastic [19]. Nominal doses were reported; however, for each experiment, the individual dose measurements obtained were within 5% of the nominal dose.

Cells, following radiation procedures, were typically transferred to sterile centrifuge tubes and maintained at 37°C for various incubation intervals as indicated.

PCC Assay

The lymphocytes were fused with CHO mitotic cells in the presence of polyethylene glycol (PEG) (MW 1450; Sigma Chemical Co., St. Louis, MO) by a modified method of *Pantelias* and *Maillie* [4] for the induction of PCC. Briefly, approximately two million mitotic cells were mixed with lymphocytes isolated from 3-4 ml of blood in a 15 ml round-bottomed glass test tube and washed with PBS. After centrifugation at 200 *g* for 8 min, the supernatant was discarded and the pellet was dried by inverting the tube over a blotting paper. The pellet was floated, being careful to keep the pellet intact, with the addition of 0.2 ml of 50% PEG (weight/volume) using a 1ml syringe. Subsequently, 2 ml of PBS was added, drop by drop in a 3 min interval, to dilute PEG; then cells were centrifuged at 200 *g* for 8 min. The pellet was resuspended in 0.4 ml of complete growth medium (KaryoMax). Colchicine (50 µl of a 10 µg/ml stock solution) and magnesium chloride (50 µl of 20 mM stock solution) was added to the cell suspension. This cell suspension was then incubated in a water bath at 37°C for 30 min. Chromosome spreads were prepared on acid-cleaned, grease-free glass slides following hypotonic treatment in 1% sodium citrate and fixation in 1:3 acetic methanol by the standard air-drying technique. Slides were stained in 4% Giemsa in distilled water for counting the number of PCC fragments under a light microscope at 1500× magnification.

Statistical Evaluation

The analysis of the yield of PCC fragments in cells for the experimental conditions described included the determination of the mean ± SE and evaluation of the frequency distribution using the σ^2/y and μ *Papworth* test [20]. Using the *Papworth* test, values of $\sigma^2/y \geq 1$ and $\mu \geq 1.96$ indicate overdispersion.

Student's *t*-test was used to compare the yield of Q_{pcc} for the partial-body studies and a χ^2 test was performed to compare observed dose estimates with those expected.

Automated Metaphase-Finder

Slides with PCC samples were evaluated with an automated metaphase-finding system (LAI Metafind, Loats Associates Inc., Westminster, MD). This system consisted of a standard cytogenetic microscope equipped with 15 slide capacity stage, motorized x-, y-, and z-axis computer-controlled positioning with specially adapted autofocus capabilities. Spread acquisition was obtained using a color camera and color digitizer board. Image display was accomplished using a 1024-line resolution video monitor. The system was controlled with customized software for automated spread localization, quality control checks and verification on a 486/66 personal computer.

Results and Discussion

The analysis of radiation-induced damage was performed in nonstimulated human lymphocytes by the PCC assay [4, 11, 12, 21]. Table I shows the results of repeated dose-response studies following exposure to 250 kVp x-rays

Table I. Results from 250 kVp x-ray dose-response studies measuring excess PCC fragments in human lymphocytes after one day of repair[a]

Dose, Gy	n	Excess PCC Fragments, Mean ± SE	σ^2/y, Ratio ± SE	μ
0	79	1.62 ± 0.32	5.12 ± 0.16	25.81
1	53	4.75 ± 0.69	5.36 ± 0.20	22.29
3	45	7.13 ± 0.69	3.04 ± 0.21	9.60
6	81	13.18 ± 0.78	3.67 ± 0.16	16.94
9	41	25.0 ± 1.78	5.11 ± 0.22	18.39

[a]Experimental conditions are described in the legend of Figure 1. Distribution analysis of the number of excess PCC fragments was analyzed as described by *Papworth* [20] using the σ^2/y and overdispersion parameter (μ). A μ value >1.96 indicates the distribution is significantly overdispersed.

and one day of repair (37°C). The number of excess PCC demonstrated a progressive increase, with dose, from 1.62 ± 0.32 at 0 Gy to 25 ± 1.78 at 9.0 Gy. These data were fitted to a linear model with a slope of 2.3 ± 0.2 excess PCC/Gy and intercept of 1.22 ± 0.63 excess PCC/Gy (r^2 = 0.968). Similar linear dose-response relationships have been observed for x-rays using human lymphocytes for doses up to 8 Gy after 1 to 24 h [12, 21].

The dose-response data of x-ray induced excess PCC fragments were also subjected to a distribution analysis using the σ^2/y and μ overdispersion test [20] (Table I). At all radiation doses the number of excess PCC fragments revealed significant overdispersion as indicated by μ values >1.96. Again the observations by *Pantelias* and *Maillie* [12] corroborate these findings since they also report significant overdispersion of lymphocyte PCC data following exposure to x-rays.

Since the distribution of PCC fragments is non-Poisson, a method that does not rely on the data demonstrating Poisson distributions was used to estimate either the irradiated fraction or dose to the irradiated fraction. We introduced the Q_{pcc}

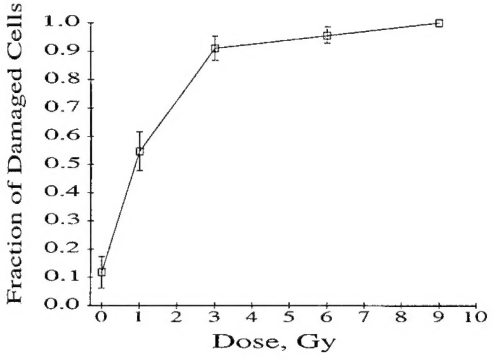

Fig. 1. Dose-response relationship for the fraction of damaged cells. Isolated human lymphocytes were exposed to 0 to 9 Gy doses of 250 kVp x-rays. Following one day of repair at 37°C, the effect of radiation on the induction of DNA damage in lymphocytes was evaluated using the PCC assay. Damaged cells represent cells with ≥48 PCC fragments per cell. Symbols reflect the mean fraction with bars representing standard errors. Data was pooled from three independent experiments.

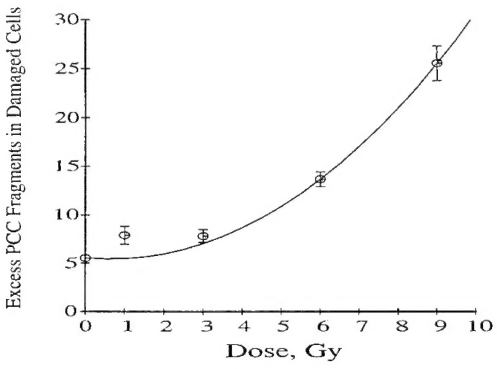

Fig. 2. Dose-response relationship for the yield of excess PCCs in damaged lymphocytes using the Q_{pcc} method. Experimental conditions are as described in the Figure 1 legend. Symbols and bars reflect the mean ± SE of excess PCC fragments in damaged cells. The curve represents a fit of the data to a weighted linear-quadratic model.

method, which is identical in concept to the Q_{dr} approach of *Sasaki* [1], and is applicable to the PCC assay for partial-body dose estimates. Damaged cells were defined as those with ≥48 PCC fragments or a suitable number in excess of nonirradiated cells. Confirmation that this approach provided a reliable indication of the size of the irradiated fraction was evidenced by the relationship of the dose dependency of the fraction of damaged cells as shown in Figure 1. These data show that the fraction of damaged cells rapidly increased with dose of radiation delivered, reaching a plateau of ≥90% damaged cells by the 3 Gy dose. These findings support the use of this approach to readily estimate partial-body fractions at high doses (>3 Gy). Recently *Darroudi* and colleagues reported successfully using this approach to accurately estimate the irradiated fraction in a partial-body primate exposure study [22].

The Q_{pcc} method also permits evaluation of the dose to the irradiated fraction. The dose dependency for the yield of excess PCC fragments in damaged cells is illustrated in Figure 2. The dose dependency of excess PCC fragments in damaged cells was fitted to a linear quadratic relationship ($Y = 5.96 + 0.046D + 0.235D^2$; D = dose in Gy, Y = excess number of PCC fragments in damaged cells) for radiation dose up to 9 Gy. This data can be used as a Q_{pcc} dose-response calibration curve to estimate dose to the irradiated fraction in simulated partial-body exposure studies.

Using in vitro 6 Gy irradiated cells, a simulated partial-body exposure study was performed. Irradiated and nonirradiated lymphocytes were mixed, following the irradiation protocol, and were incubated for one day at 37°C. The PCC assay was performed to address the potential role of interphase cell death, efficiency of PEG-mediated fusion and chromosome condensation in determining estimates of the irradiated fraction and dose to the irradiated fraction of cells in a mixed-cell culture. The fraction of damaged cells and the estimated radiation doses for different fractions of irradiated cells for this study are shown in Table II. The measured fraction of damaged cells correlated with the irradiated fraction, indicating no apparent decreased efficiency of the PCC assay on damaged cells. Using the Q_{pcc} method, the dose to the irradiated fraction was estimated based on the mean number of excess PCCs and the

Table II. Results from a mixed-cell culture study examining the ability of the PCC assay to determine the fraction of irradiated cells and dose to the irradiated fraction of cells.[a]

Mixed Culture		Sample Size		% >48 PCCs		Q_{pcc} Analysis				
% 0 Gy	% 6 Gy	Total no.	No. >48 PCCs	% (SE)	Excess PCCs in Damaged Cells, Mean (SE)	P, *t*-test	Estimated Radiation Doses, Gy Equivalent (SE)	x^2	DF	P, x^2 test
100	0	34	6	18 (6.6)	—	—	—	—	—	—
80	20	40	14	35 (7.6)	11.6 (1.9)	.267	5.3 (0.6)	.082	1	.77
70	30	40	14	35 (7.8)	10.1 (1.7)	.049	4.7 (0.6)	.282	1	.60
50	50	40	24	60 (7.8)	11.0 (1.4)	.071	5.0 (0.6)	.167	1	.68
25	75	40	32	80 (6.4)	10.8 (1.4)	.042	4.7 (0.8)	.282	1	.60
0	100	81	78	96 (2.1)	13.7 (2.1)	—	6.0 (0.2)	—	—	—

[a]Experimental conditions for the mixed-culture study were as described in the Results and Discussion section. The excess number of PCC fragments in damaged cells was compared with the results from the 100% 6-Gy sample using Student's *t*-test. Estimated radiation doses were determined by using measured values of excess PCC fragments and the Q_{pcc}-standard dose-response curve. The resultant predicted dose-equivalent values were compared with the expected value of 6-Gy using the x^2 test. The x^2 *P* value for the pooled results was 0.94.

Fig. 3. Photograph of a video monitor image demonstrating the use of automated metaphase-finding system for locating PCC spreads. The customized metaphase software uses gray-scale morphometric algorithms to isolate candidate metaphase spreads, based on geometric shape, spread density and texture measurements. Candidate spreads are displayed in a postage-stamp format for user review of spread quality or, as in this case, for identification of PCC spreads for analysis. User-chosen spreads are automatically located on the slide and displayed at high power for analysis on a high-resolution monitor.

Q_{pcc}-dose-response calibration curve. Dose estimates ranged from 4.7 to 5.3 Gy for the 0% to 75% irradiated volume and were not significantly different from those expected at the 6 Gy dose (pooled Chi^2 $P = 0.94$).

Investigators earlier addressed the problem of cell selection, interphase death and mitotic delay leading to the underestimation of the radiation dose in the event of partial-body exposure by the conventional dicentric assay [23, 24]. For x-rays from 1 to 10 Gy and ratios of irradiated and nonirradiated blood from 1:1 to 1:9, agreement was found between calculated and applied radiation doses and fractions exposed by use of the contaminated Poisson method on dicentric data by *Hilali* and colleagues [14]. However, this approach is very dependent on scoring of a large number of samples (>500 metaphase spreads), which can be difficult in the case of accidental high-dose radiation overexposures.

Our studies demonstrated the potential advantages of the PCC assay to aid in overcoming some of the complex problems (e.g., mitotic delay, interphase death and failure of stimulation) that interfere with dose estimation in the lymphocyte dicentric assay. At very high radiation doses (>9 Gy) with significant reductions in lymphocyte peripheral blood counts, the PCC assay may provide an underestimation of the radiation dose to the irradiated fraction without correcting the results for loss of heavily damaged cells from the circulating peripheral blood pool.

Rapid localization of the PCC spreads on the slide is desired to expedite the visual enumeration of PCC fragments. Use of an automated metaphase-finding system can facilitate the localization and scoring of the PCC spreads, since the yield of PCCs is relatively low compared to the mitotic inducer cells and lymphocytes.

Using the search program of the metaphase-finding software under a low-power (10×) objective, PCCs were readily detected amidst the metaphase spreads and were displayed in a postage-stamp mode following automatic

scanning of the slides (Fig. 3). The metaphase-finding software also conveniently repositions the microscope stage to permit reexamination of specific PCCs at higher magnification by selecting identified postage-stamp images of PCC spreads. Typical slide-scanning times of ≤20 min per slide, to obtain a threshold of 150 metaphase spreads, were observed. The automated finding of candidate metaphase spreads significantly increased the speed of scoring PCCs.

Efforts are under way to automate the counting of the PCC fragments in our laboratory. *Pantelias* and colleagues [25] recently applied C-banding techniques to the PCC assay, permitting the scoring of dicentrics and centric rings in these preparations. Similar capabilities can be obtained using in situ DNA hybridization methodology [7, 26] applied to PCC samples. Application of these chromosome-painting techniques to permit measurement of chromosome aberrations typically associated with radiation injury and the use of automated scoring systems can assist cytogeneticists in providing biodosimetry information rapidly to clinicians treating radiation victims following acute exposures.

Acknowledgments

The authors acknowledge and thank *E. A. Blakely, G. E. Iliakis,* and *A. T. Natarajan* and colleagues for assistance in establishing the PCC assay in our laboratory. We also thank *Paul J. Emanuel* for his help in the x-ray irradiation procedures and dosimetry, and *W. E. Jackson* for his expert statistical assistance. The authors wish to acknowledge helpful comments by *D. M. Bauchinger* and *D. van Beuningen,* and expert editorial assistance by *D. K. Solyan*. This research was supported by the Armed Forces Radiobiology Research Institute, under work unit number 04640. This work was performed while one author, *P. G. S. Prasanna,* held a National Research Council (AFRRI) Research Associateship. The views presented are those of the authors; no endorsement by the Armed Forces Radiobiology Research Institute has been given or should be inferred.

References

1 Sasaki, MS. Use of lymphocyte chromosome aberrations in biological dosimetry: possibilities and limitations. In: Ishihara T, Sasaki MS, eds. Radiation-Induced Chromosome Damage in Man. New York: Alan R. Liss, Inc., 1983:585-604.

2 Johnson RT, Rao PN. Mammalian cell fusion: induction of premature condensation in interphase nuclei. Nature 1970;226:717-722.

3 Okayasu R, Cheong N, Iliakis G. Comparison of yields and repair kinetics of interphase chromosome breaks visualized by Sendai-virus or PEG-mediated cell fusion in irradiated CHO cells. Int J Radiat Biol 1993;64:689-694.

4 Pantelias GE, Maillie HD. A simple method for premature chromosome condensation induction in primary human and rodent cells using polyethylene glycol. Somat Cell Genet 1983;9:533-547.

5 Hittleman WN, Sognier MA, Cole A. Direct measurement of chromosomal damage and its repair by chromosome condensation. In: Meyn RE, Withers HR, eds. Radiation Biology in Cancer Research. New York: Raven Press, 1980:103-123.

6 Cornforth MN, Bedford JS. x-ray-induced breakage and rejoining in human interphase chromosome. Science 1983;222:629-630.

7 Goodwin E, Blakely E, Ivery G et al. Repair and misrepair of heavy-ion-induced chromosomal damage. Adv Space Res 1989;9(10):83-89.

8 Suzuki M, Watanabe M, Suzuki K et al. Heavy ion-induced chromosome breakage studies by premature chromosome condensation (PCC) in Syrian hamster embryo cells. Int J Radiat Biol 1992;62:581-586.

9 Loucas BD, Geard CR. Kinetics of chromosome rejoining in normal human fibroblasts after exposure to low- and high-LET radiations. Radiat Res 1994;138:352-360.

10 Bedford JS, Goodhead DT. Breakage of human interphase chromosomes by alpha particles and x-rays. Int J Radiat Biol 1989;55:211-216.

11 Pantelias GE, Maillie HD. The measurement of immediate and persistent radiation-induced chromosome damage in rodent primary cells using premature chromosome condensation. Health Phys 1985;49(3):425-433.

12 Pantelias GE, Maillie HD. Direct analysis of radiation-induced chromosome fragments and rings in unstimulated human peripheral blood lymphocytes by means of the premature chromosome condensation technique. Mutat Res 1985;149:67-72.

13 Lloyd DC, Edwards AA, Prosser JS et al. A collaborative exercise on cytogenetic dosimetry for simulated whole and partial body accidental irradiation. Mutat Res 1987;179:197-208.

14 Hilali A, Leonard ED, Decat G et al. An appraisal of the value of the contaminated Poisson method to estimate the dose inhomogeneity in simulated partial-body exposure. Radiat Res 1991;128:108-111.

15 Natarajan AT, Darroudi F, Ramalho AT. Cytogenetic indicators of radiation exposure. In: MacVittie TJ, Weiss JW, Browne D, eds. Advances in the Treatment of Radiation Injuries (April 1993, Bethesda, MD, USA). Oxford, England: Pergamon Press (in press).

16 Lloyd DC. An overview of radiation dosimetry by conventional cytogenetic methods. In: Eisert, WG, Mendelsohn ML, eds. Biological Dosimetry. Berlin Heidelberg: Springer-Verlag, 1984:3-14.

17 Sevan'kaev AV, Tsyb AF, Lloyd DC et al. 'Rogue' cells observed in children exposed to radiation from the Chernobyl accident. Int J Radiat Biol 1993;63:361-367.

18 Holahan EV, Blakely WF, Walden TL. Effect of PGE_2 on radiation response of Chinese hamster V79 cells in vitro. In: Walden TL, HN Hughes, eds. Prostaglandin and Lipid Metabolism in Radiation Injury. New York: Plenum Press, 1987:253-262.

19 ICRP Report 23. Measurements of absorbed dose in a phantom irradiated by a single beam of x or gamma rays. Washington, DC, USA: ICRU Publications, 1973:1-30.

20 Papworth DG (Appendix to paper by JRK Savage). Sites of radiation-induced chromosome exchanges. Curr Top Radiat Res 1970;6:129-194.

21 Vyas RC, Darroudi F, Natarajan AT. Radiation-induced chromosomal breakage and rejoining in interphase-metaphase chromosomes of human lymphocytes. Mutat Res 1991;249:29-35.

22 Darroudi F, Natarajan AT, Broerse JJ et al. Biological dosimetry and monitoring following in vivo exposure to X-irradiation. In: Programme and Abstract Book of the European Society of Radiation Biology (June 1994, Amsterdam, The Netherlands). 1994:116.

23 Fabry L, Leonard A, Decat G et al. Chromosome aberrations in mixed cultures of in vitro irradiated and unirradiated human lymphocytes. Strahlenther und Onkol 1988;164:108-110.

24 Poncelet E, Leonard A, Leonard ED et al. Biological dosimetry: radiation-induced mitotic delay can lead to an underestimate of the part of the body exposed after non-uniform irradiation. Strahlenther und Onkol 1988;164:542-543.

25 Pantelias GE, Iliakis GE, Sambani CD et al. Biological dosimetry of absorbed radiation by C-banding of interphase chromosomes in peripheral blood lymphocytes. Int J Radiat Biol 1993;63:349-354.

26 Evans JW, Chang JA, Giaccia AJ et al. The use of fluorescence in situ hybridisation combined with premature chromosome condensation for the identification of chromosome damage. Br J Radiol 1991;63:517-521.

J. RADIAT. RES., 36, 77–90 (1995)

Effect of Antihistamines, Disodium Cromoglycate (DSCG) or Methysergide on Post-irradiation Cerebral Blood Flowand Mean Systemic Arterial Blood Pressure in Primates after 25 Gy, Whole-body, Gamma Irradiation[1]

L. G. COCKERHAM AND C. D. FORCINO

Physiology Department, Armed Forces Radiobiology
Research Institute, Bethesda, Maryland 20889–5603
(*Received, December 1, 1993*)
(*Revision Received: March 1, 1995*)
(*Accepted: March 3, 1995*)

Histamine/Hypotension/Ischemia/Radiation/Serotonin

Exposure to ionizing radiation causes hypotension, cerebral ischemia and release of histamine (HA) and serotonin (5-HT). To investigate the relationship among these responses, rhesus monkeys (*Macaca mulatta*) received physiological saline (i.v.), disodium cromoglycate (DSCG), antihistamines (AH, mepyramine and cimetidine), or methysergide (METH), then were given 25 Gy whole-body irradiation. Monkeys receiving DSCG, AH or METH had higher post-irradiation mean arterial blood pressure (MBP) than saline-treated controls. Compared to levels in controls, post-irradiation hippocampal blood flow (rCBF) levels were higher in monkeys receiving DSCG, AH or METH. Treatment with the 5-HT_2 receptor antagonist methysergide was the most effective in maintaining both rCBF and MBP after irradiation. Results support the hypothesis that the irradiation-induced cerebral ischemia and, to some extent, the hypotension is mediated by serotonin through 5-HT_2 receptor sites.

---

[1] Address all correspondence to: Dr. Lorris G. Cockerham. *Phenix Consulting & Services Ltd. Co.* 3006 Hinson Road, Little Rock, AR 72212–2712, U.S.A.
Supported by the Armed Forces Radiobiology Research Institute, Defense Nuclear Agency, under work unit 00053 in 1986. Views presented in this paper are those of the authors; no endorsement by the Defense Nuclear Agency has been given or should be inferred. Research was conducted according to the principles enunciated in the "Guide for the Care and Use of Laboratory Animals" prepared by the Institute of Laboratory Animal Resources, National Research Council.

INTRODUCTION

Studies have shown elevated levels of circulating blood histamine (HA) in humans undergoing radiation therapy[1] and increased levels of HA in plasma of nonhuman primates[2,3] following irradiation. HA is implicated in irradiation-induced hypotension and post-irradiation reduced cerebral blood flow[2,4]. However, HA is not the only biological mediator involved in irradiation injury[5,6] and may not be the mediator directly responsible for the irradiation-induced decrease in cerebral blood flow[7,8].

The irradiation-induced reduction in cerebral blood flow may employ intermediate mediators such as free radicals produced by exposure to ionizing irradiation[9–11]. Free radical interactions are implicated in many pathological conditions including irradiation injury, ischemia, microvascular injury and cell membrane damage[12–15]. Disodium cromoglycate (DSCG), a known mast-cell stabilizer and an efficient free-electron scavenger[5,16], was employed successfully to diminish the irradiation-induced decrease in regional cerebral blood flow (rCBF) without altering significantly the irradiation-induced release of HA[4]. However, DSCG and the antihistamines (AH) mepyramine and cimetidine, given in combination, significantly altered post-irradiation hypotension and the reduction in rCBF[2]. Therefore, a hypothesis that attempts to explain the irradiation-induced hypotension and reduced rCBF solely through the free electron-histaminergic mechanisms may be incorrect.

Serotonin (5-hydroxytryptamine, 5-HT) is released after irradiation[5,6] and causes contraction of vascular smooth muscle by direct and indirect actions[17–19]. Intracarotid infusion of neurotensin into the isolated, perfused head of rats triggered 5-HT and HA release within one minute and elicited vasoconstriction[20]. The vasoconstrictor response was greatly attenuated by the 5-HT receptor antagonist methysergide (METH) but unaffeted by the antihistaminic drugs mepyramine and cimetidine. This suggests that the vasoconstriction was mediated by 5-HT rather than by HA.

In an attempt to elucidate mechanisms underlying the irradiation-induced decrease in rCBF in primates, the effects of AH, DSCG or METH on post-irradiation hippocampal blood flow (rCBF) and mean systemic arterial blood pressure (MBP) were compared after a bilateral whole body irradiation of animals corresponding to a midline tissue dose of 25 Gy of ^{60}Co gamma rays. The hippocampus was selected as the region of interest because this area of the brain is particularly vulnerable to oxygen deprivation associated with ischemia[21,22] and shows alteration of neuronal activity following irradiation[23–25].

MATERIALS AND METHODS

In this study we used 22 male rhesus monkeys (*Macaca mulatta*) weighing between 3.0 kg and 3.9 kg (3.25 ± 0.06 SEM). The animals were divided randomly into four groups: (1) six given physiological saline (i.v.) for 60 minutes before and after irradiation, (2) six given mepyramine (0.5 mg/min, i.v.) and cimetidine (0.25 mg/min, i.v.) in saline for 60 minutes before and after

irradiation, (3) four given DSCG (100 mg/kg, i.v.) five minutes before irradiation, and (4) six given methysergide orally (4 mg/day) for two days before irradiation and by infusion (0.476 μg/kg/min, i.v.) in saline for 60 minutes before and 60 minutes after irradiation. Food was withheld from all animals for 18 hours before the experiment, but water was available *ad libitum*. Research was conducted according to the principles enumerated in the *Guide for the Care and Use of Laboratory Animals* prepared by the Institute of Laboratory Animal Resources, National Research Council (U.S.A.). Monkeys were initially anesthetized in their cages with ketamine hydrochloride (20 mg/kg, i.m.) supplemented with 0.015 mg/kg atropine sulfate, and were then moved to the laboratory for the remainder of the experiment.

A systemic venous catheter was used to administer physiological saline and the principal anesthetic, α-Chloralose (100 mg). Supplemental infusions were provided as needed, based on heart rate, blood pressure, blood pH, and peripheral reflexes. A femoral arterial catheter was used to withdraw blood for blood gas determinations and to measure systemic arterial blood pressure.

Approximately 2 hours before irradiation, the animals were intubated with a cuffed endotracheal tube and ventilated using a forced volume respirator to maintain stable blood pH and oxygen tension. After insertion of the endotracheal tube each animal was placed on a circulating water blanket to maintain body temperature between 36°C and 38°C. A rectal probe monitored body temperature.

Using a technique previously described[2,4,7], platinum-iridium wire electrodes were placed in the left and right hippocampi (CA1 region) to measure rCBF by hydrogen clearance. Measurements were taken for 30 minutes before irradiation and for 60 minutes after. This technique is essentially an amperometric method that has been successfully employed in similar studies[2,4,7,8].

After 30 minutes of pre-irradiation measurements the animals were disconnected from the respirator and recording apparatus and irradiated in a separate room, using a bilateral, whole-body exposure to gamma ray photons from a ^{60}Co source located at the Armed Forces Radiobiology Research Institute. All doses quoted are midline abdomen tissue doses. Prior to animal irradiations the midline abdomen tissue (MLAT) dose rate was measured by placing a 0.5 cc tissue equivalent ionization chamber (calibration factor traceable to the National Institute of Standards and Technology) at the center of a 23.6 cm diameter, cylindrical acrylic phantom, 28 cm in length. Exposure time was adjusted so that each animal received a total 25 Gy MLAT at a nominal dose rate of 47 Gy per minute. The tissue-to-air ratio (TAR), defined as the ratio of the dose rate in free air to the dose rate measured in the phantom, was 0.95. The techniques used for these measurements were in accordance with the AAPM protocol for the determination of absorbed dose from high-energy photon and electron beams[26]. [The Gray (Gy), the Système Internationale (SI) unit for absorbed dose, corresponds to an energy absorption of 1 J/kg or 100 rad.]

The animals were reconnected to the respirator and recording apparatus at 4 minutes post-irradiation and measurements were continued for a minimum of 60 minutes. At 30 and 10 minutes before irradiation, and at 2, 4, and 6 minutes after irradiation, blood samples were taken via the arterial catheter to monitor stability of blood pH and oxygen tension, and

respiration was adjusted to maintain pre-irradiation levels. MBP was determined via the arterial catheter during the experiment. After the experiment, the animals were humanely euthanized with an i.v. injection of saturated $MgSO_4$ while still under anesthesia. Brains were removed and dissected for visual verification of electrode placement.

Blood pressure and blood flow data were grouped into 10 minute periods, measured in relation to midtime of radiation. Data from each period were averaged and plotted at the middle of the period. The Shapiro-Wilk Test was used to assess normality of values of the various sample groups[27]. The Wilcoxon Rank Sum Test[28] was used for the statistical analysis of the blood pressure and blood flow data. A 95% level of confidence was employed to determine significance. Because all animals were treated identically before irradiation, and because the data for control and test animals showed no significant difference among monkeys at 30 minutes and 10 minutes before irradiation, pre-irradiation data were combined for each monkey.

Table 1. Abbreviation and Acronym Definitions

5-HT	=	5-Hydroxytryptamine, Serotonin
AAPM	=	American Association of Physicists in Medicine
AH	=	Antihistamines
CBF	=	Cerebral Blood Flow
DSCG	=	Disodium Cromoglycate
Gy	=	Gray, SI unit for absorbed dose
HA	=	Histamine
MBP	=	Mean Arterial Blood Pressure
METH	=	Methysergide
MLAT	=	Midline Abdomen Tissue
rCBF	=	Regional Cerebral Blood Flow
SEM	=	Standard Error of the Mean
SI	=	Système Internationale
TAR	=	Tissue-to-Air Ratio

RESULTS

The Shapiro-Wilk test, which assesses the composite hypothesis of normality[27], indicated that data from many samples were sufficiently inconsistent ($p<0.05$) with a normal distribution. This finding encouraged us to use alternate methods, such as distribution-free techniques or non-parametric statistical procedures[27]. Therefore, the Wilcoxon Rank Sum Test was used for the final statistical analysis[28].

The mean systemic arterial blood pressure (MBP) of the four groups of irradiated animals decreased from the pre-irradiation mean of 106 ± 3.4 mm Hg within 10 minutes after irradiation (Figure 1 and Table 2). The irradiated group given saline showed a drop only to the 10 minutes post-irradiation level that was approximately 35% of the pre-irradiation value. The irradiated group treated with DSCG showed blood pressure levels that dropped to approximately the same

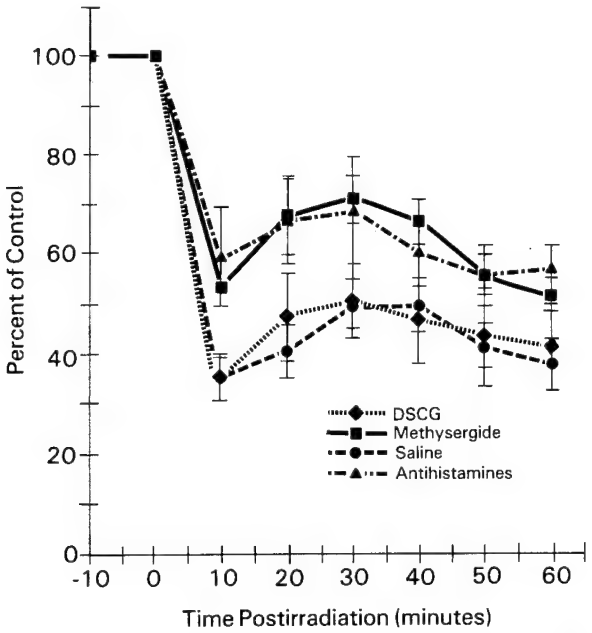

Figure. 1. Percent of preirradiation mean arterial blood pressure (MBP) after exposure to 25 Gy, whole-body, gamma irradiation (±SEM), compared to a preirradiation mean of 106.0±3.4 mm Hg. Six animals were given physiological saline for 60 min before and after irradiation. One group (n=4) received the saline infusion for 60 min before and after irradiation, and disodium cromoglycate (DSCG) by i.v. infusion (100 mg/kg) 5 min before irradiation. The third group (n=6) received the antihistamines (AH) mepyramine (0.5 mg/min) and cimetidine (0.25 mg/min) in the saline infusion for 60 min before and after irradiation. The fourth group (n=6) received methysergide (METH) orally (4 mg/day) for two days before irradiation and by infusion (0.476 μg/kg/min, i.v.) in saline for 60 min before and after irradiation.

Table 2. Percent of Preirradiation Mean Arterial Blood Pressure (MBP) After Exposure to 25 Gy, Whole-Body, Gamma Irradiation[a].

Time (min) Post-irradiation	Treatment			
	Saline	DSCG	AH	METH
10	35.20±4.31	35.50±4.72	59.60± 9.86	53.43±6.15*
20	40.67±5.34	47.50±8.74	66.80± 8.73	67.43±7.55*
30	50.17±5.03	51.00±7.30	68.80±10.69	71.00±4.70*
40	50.00±5.33	47.00±8.49	60.60± 6.93	66.57±4.17*
50	42.00±4.41	43.75±9.72	56.00± 5.96	56.14±3.92*
60	38.17±4.95	41.75±8.62	57.40± 4.57	52.14±3.33*

* Significantly different from saline treated ($p \leq 0.05$)

* Mean ± SEM

levels (36%) as those treated with saline only. The group treated with AH showed blood pressure levels that dropped to approximately 60% of the pre-irradiation mean while the group treated with METH showed a decline to 53.43% of the pre-irradiation mean. However, the METH treated group was the only group to show a significant difference between its post-irradiation MBP values and those of the saline treated group. A significant difference ($p \leq 0.05$) was seen between the MBP values of the METH treated group of monkeys and the saline treated group at any time after irradiation. In each of the four groups, the respiration of each subject was maintained at pre-irradiation levels, and the blood gas data revealed a general stability of blood pH and oxygen tension throughout the experiment (data not shown).

Within 10 min post-irradiation, blood flow values for the saline treated animals showed a rapid, significant decline to approximately 53% of the pre-irradiation levels of 75.1 ± 5.9 ml per

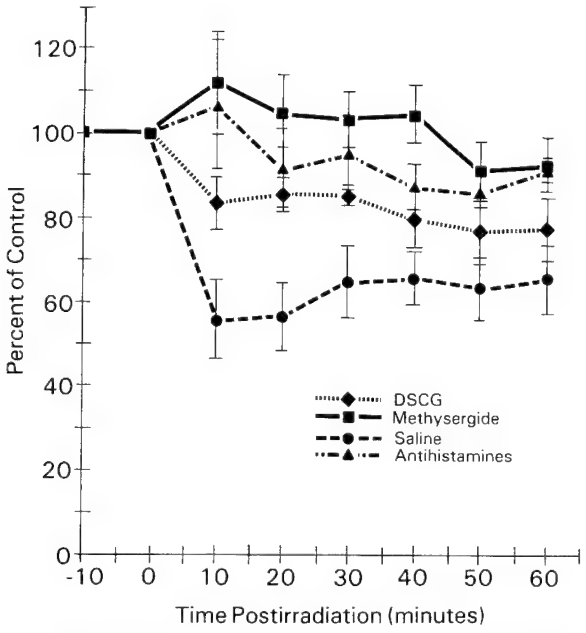

Figure. 2. Percent of preirradiation mean hippocampal blood flow (rCBF) after exposure to 25 Gy, whole-body, gamma irradiation (±SEM), compared to a preirradiation mean of 75.1 ± 5.9 ml/100 g of tissue/min. Six animals were given physiological saline for 60 min before and after irradiation. One group (n=4) received the saline infusion for 60 min before and after irradiation, and disodium cromoglycate (DSCG) by i.v. infusion (100 mg/kg) 5 min before irradiation. The third group (n=6) received the antihistamines (AH) mepyramine (0.5 mg/min) and cimetidine (0.25 mg/min) in the saline infusion for 60 min before and after irradiation. The fourth group (n=6) received methysergide (METH) orally (4 mg/day) for two days before irradiation and by infusion (0.476 αg/kg/min, i.v.) in saline for 60 min before and after irradiation.

Table 3. Percent of Preirradiation Mean Hippocampal Blood Flow (rCBF) After Exposure to 25 Gy, Whole-Body, Gamma Irradiation[a].

Time (min) Post-irradiation	Treatment			
	Saline	DSCG	AH	METH
10	52.83±9.28	83.50±6.45	106.6±15.18*	111.86±12.36**
20	56.67±7.89	85.50±4.13	91.6± 9.23*	105.29± 8.39**
30	64.83±8.44	85.25±2.39	95.0± 8.07*	103.14± 6.66**
40	66.00±6.44	79.50±6.44	87.4± 5.36*	104.29± 6.96**
50	63.33±7.54	77.25±7.95	86.4± 3.75*	91.00± 6.78*
60	65.67±7.98	77.50±7.35	91.4± 2.91*	92.71± 6.54*

* Significantly different from saline treated ($p \leq 0.05$)
** Significantly different from saline treated ($p \leq 0.01$)
[a] Mean ± SEM

100 g of tissue per min in the hippocampus (Figure 2, Table 3). At all measurements after irradiation, rCBF was not significantly different between the saline and DSCG groups. The remaining two groups of irradiated animals (one given AH and the other given METH) did not show initial decreases in rCBF and were significantly different ($p \leq 0.05$) at all post-irradiation measurements from the group given saline. In fact, after irradiation, rCBF levels for both the AH and the METH treated groups showed increases within two minutes to levels that were higher than the pre-irradiation levels. The rCBF in the AH treated group decreased to a level less than the pre-irradiation level by the 20-min post-irradiation observation, but remained significantly different ($p \leq 0.05$) from the levels in the saline treated group for the remainder of the experiment. However, the rCBF in the METH treated group did not decrease to a level less than the pre-irradiation level until after the 40-min post-irradiation observation and was significantly different ($p \leq 0.01$) from the levels in the saline treated group during this time.

DISCUSSION

The initial precipitous decline in post-irradiation MBP and rCBF reported here has been well documented in other studies of the rhesus monkey[2,4,7,8,29]. The immediate post-irradiation decrease in rCBF is usually associated with the decline in the MBP since it is thought that a critical MBP of 50% to 60% of normal is necessary in primates for adequate autoregulation of cerebral circulation[29–31].

The inability of DSCG to alter significantly the post-irradiation hypotension when given alone corroborates a previous report[4] in which there was not a significant difference between the post-irradiation MBP of DSCG-treated monkeys and the post-irradiation MBP of saline-treated monkeys. However, in contrast to the previous report, this study does not show a statistically significant difference in post-irradiation rCBF between the DSCG-treated group of monkeys and the saline-treated group of animals. The only treatment difference between the previous report and this report was the level of irradiation. Monkeys in the previous experiment were exposed to

100 Gy, whole body, γ irradiation while the animals in this experiment were exposed to 25 Gy, whole body, γ irradiation. This comparison may then suggest a dose dependent variation resulting in a significant difference in post-irradiation rCBF at a high dose but not at a relatively lower dose.

Another influence on the statistical significance of the difference between rCBF in the saline treated group and the DSCG group was the number of animals in the latter group. Since DSCG had been successfully employed to alter post-irradiation rCBF in a previous experiment[4] only four animals were assigned to the group to be treated with DSCG. The inconsistency of data indicated by the Shapiro-Wilk test[27], when applied to these four animals, probably contributed to the lack of statistical significance between the saline treated group and the DSCG treated group in Table 3. Therefore, even though the difference looks biologically significant, it is not statistically significant.

The regional brain concentration of biological mediators such as catecholamines, histamine, serotonin and the eicosanoids may be a third factor playing an important role in rCBF response to irradiation. For example, the two regions selected for study in the previous report[4] vary dramatically in mast cell and histamine content and responded differently to irradiation and to the administration of DSCG. The hypothalamus contains numerous mast cells and the highest histamine concentrations in the brain[32-34] while the postcentral gyrus is an area with few mast cells and little histamine[32,33].

The addition of the H_1 and H_2 receptor blockers, mepyramine and cimetidine, in combination with DSCG, resulted in an alteration of the post-irradiation MBP not achieved with the administration of DSCG alone[2]. Animals given the mast cell stabilizer DSCG and the antihistamines before and after irradiation did not exhibit an abrupt decline in blood pressure but displayed a gradual decrease in MBP below pre-irradiation levels. Also, the treated, irradiated monkeys displayed rCBF values that were not significantly different from the non-irradiated controls. Since post-irradiation rCBF and MBP were not measured in primates given the antihistamines without DSCG, before and after irradiation, it was difficult to determine if it was the DSCG or the antihistamines that was responsible for the response.

Monkeys given the antihistamines mepyramine and cimetidine before and after irradiation in this experiment showed higher MBP and rCBF than those given either saline or DSCG. The post-irradiation mean rCBF of the antihistamine treated group was significantly different ($p \leq 0.05$) from that seen in the saline treated group. Although the post-irradiation MBP of the antihistamine treated monkeys was not statistically different from that of the saline treated monkeys, the difference may have been biologically significant because of the effect hypotension may have on cerebral blood flow. Besides the potential for HA to alter rCBF through its hypotensive actions, HA is also a direct acting cerebral vasodilator when applied *in vitro* or topically[34]. Furthermore, infusing HA into humans resulted in decreased MBP and altered rCBF[35,36]. However, in another study, similar treatment altered neither MBP nor rCBF[37]. Therefore, the net effect of small concentrations of HA or rCBF is unclear. In any case, the antihistamines were more effective than DSCG in blocking the hypotensive and reduced rCBF responses to irradiation.

The greater effectiveness of the antihistamines may be due to cimetidine, a specific

histamine H_2 antagonist, which blocked the immediate bradycardia and hypotension caused by intravenous injection of serotonin[38]. Furthermore, the hypotensive effect of 5-HT infusion is likely due to an action in the cell body regions of the raphe nuclei[39]. This suggests that a post-irradiation release of serotonin, and not histamine, may be directly responsible for the irradiation-induced decrease in rCBF since serotonin is normally released after irradiation[5,6,40] and causes contraction of vascular smooth muscle by direct and indicrect actions[17–19]. Indeed, Rioux *et al*[20], has shown with the isolated, neurotensin-perfused head of the rat that it is not the release of histamine that may be responsible for a decreased rCBF, but the release of serotonin. This agrees with an earlier report by Edvinsson and Owman[41] that serotonin is the most efficient vasoconstrictor agent for human pial arteries with its effect inhibited by the serotonin antagonist, methysergide.

In this experiment MBP followed a triphasic pattern consisting of an initial reflex hypotension, a secondary pressor response and a delayed hypotension in all four groups of monkeys (Figure 1, Table 2). However, the post-irradiation hypotension was altered significantly ($p \leq 0.05$) with the administration of methysergide (METH). A possible explanation for the action of METH is that it is a selective 5-HT_2 antagonist[42] and 5-HT is implicated in coronary artery constriction and reduced coronary blood flow[19]. This could contribute to irradiation-induced cardiovascular dysfunction[43] resulting in a decreased cardiac output and post-irradiation hypotension. However, Freed *et al*[39] concluded that it is brain serotonin rather than serotonin in heart or other peripheral tissues which causes the hypotension.

The serotonin antagonist, methysergide, was the most effective agent used in this study to block the irradiation-induced decrease in rCBF (Figure 2, Table 3). Hippocampal blood flow in the METH treated monkeys actually increased above the pre-irradiation mean for 40 min post-irradiation and was significantly different ($p \leq 0.01$) from the rCBF in the saline treated group for that time. For the last 20 min of the measurements, the rCBF of the METH treated animals remained significantly different ($p \leq 0.05$) from the rCBF of the saline treated group, although falling slightly below the pre-irradiation level. These results are consistent with a cerebrovascular vasoconstrictor role for serotonin and suggest serotonin involvement in the irradiation-induced decrease in rCBF.

Serotonin has a complex action in the cerebrovasculature, causing contraction or relaxation depending on the species involved, the cellular structure first encountered and the type of 5-HT receptors present[17,18,42,44]. Serotonin receptors may be subdivided into at least six subtypes called 5-HT_{1A}, 5-HT_{1B}, 5-HT_{1C}, 5-HT_{1D}, 5-HT_2 and 5-HT_3[42]. Vascular constriction is mediated primarily through the 5-HT_2 receptors with some 5-HT_1 involvement[45]. 5-HT_1 receptors are involved primarily with arteriolar dilatation. Other proposed functional correlates of 5-HT_1 receptor subtypes are dorsal raphe cell and CA1 hippocampal cell inhibition, thermoregulation, and hypotensive effects[42].

Emesis is a common symptom of the early prodromal phase of radiation sickness in humans[46] and the ferret has proven an excellent small animal model for the study of irradiation-induced emesis[47,48]. The area postrema has been implicated in irradiation-induced emesis[49] and specific 5-HT_3 binding sites have been shown in the brains of several species, including humans and ferrets[50]. The use of 5-HT_3 receptor antagonists such as ondansetron, granisetron, zacop-

ride and Y-25130 in controlling irradiation-induced emesis[51–55] further strengthened the relationship between 5-HT and some of the pathophysiological results of irradiation.

In contrast to the subtypes of the 5-HT_1 and 5HT_3 sites, 5HT_2 sites are quite homogeneous[42]. The highest concentration of 5-HT_2 binding sites in the brain are in the caudate and layer IV of the cerebral cortex where the application of 5-HT caused a slow depolarization of cortical neurons, resulting in decreased conductance. Proposed functional correlates of 5-HT_2 receptor subtypes include contraction of vascular smooth muscle, contraction of bronchial smooth muscle, head twitches seizuers and edema. Infusion of 5-HT produced brain edema, increasd blood-brain barrier permeability and decreased rCBF, all of which can be prevented with a 5-HT_2 receptor antagonist[56,57].

Serotonin also may be associated with impairment of CBF autoregulation as shown with renal autoregulation in the low pressure range[58]. In fact, no correlation was seen between MBP and CBF as demonstrated by red cell velocity after intracarotid injection of 5-HT even though correlation existed between MBP and CBF following arterial blood withdrawal[59]. However, following exposure to moderate irradiation (4 Gy) with ^{137}Cs, ferrests showed no significant change in MBP but a general reduction of rCBF ranging from 7 to 33%[47]. Certainly, the involvement of 5-HT in autoregulation of CBF following irradiation is still a matter of discussion requiring further investigation.

Many of the sequelae of 5-HT adminstration are similar to the results of irradiation[60–62], notably hypotension, emesis, brain edema, altered blood-brain barrier permeability and a marked reduction in rCBF as well as total CBF. As noted before, some of these can be prevented with the proper selective 5-HT receptor antagonist. Irradiation-induced emesis can also be altered with the proper 5-HT_3 receptor antagonist. This study reports the amelioration of irradiation-induced hypotension and diminished rCBF in the hippocampus with the 5-HT_2 receptor antagonist, methysergide and the greater effectiveness of methysergide compared to the antihistamines mepyramine and cimetidine, and the mast cell stabilizer, disodium cromoglycate, in this action. We believe that these results, although not conclusive, support the hypothesis that irradiation-induced diminished hippocampal blood flow and, to some extent, post-irradiation hypotension is mediated by 5-HT through 5-HT_2 receptor sites.

The phenomenon of CNS radiation abnormalities and damage that are not associated with the tumor under treatment but occur with the radiotherapy has been well documented but remains poorly understood[63–66]. Necrosis in the tissue surrounding the tumor may be secondary to radiation-induced edema and ischemia and the cerebrovasculature of the normal parenchyma may be more sensitive to the effects of cranial irradiation than that found in the tumor[66,67]. There is now increased interest in the possible use of agents which might limit irradiation-induced changes in cerebral blood flow and the extent of tissue injury[68,69]. We suggest that the use of a 5-HT_2 receptor antagonist will not only diminish the irradiation-induced alteration in cerebral blood flow, thereby ameliorating the associatied pathologic changes in tissue surrounding the tumor, but also may improve the blood flow in tumors under radiotherapy and alter the response of the radioresistant hypoxic cells that have been shown to occur in nearly all animal tumors and may exist in some human cancers[68,70].

These results and conclusions were communicated in part at the Cerebral Hypoxia and

Stroke Symposium, Budapest, Hungary, August 22-24, 1987[71] and at the NATO Adavanced Study Institute on Terrestrial Space Radiation and It's Biological Effects, Corfu, Greece, October 11–25, 1987[72].

ACKNOWLEDGMENTS

The authors thank Dr. T. C. Pellmar, Ms S. W. Smart and Mr. E. J. Golightly for technical assistance.

REFERENCES

1. Lasser, E. C. and Stenstrom, K. W. (1954) Elevation of circulating blood histamine in patients undergoing deep roentgen therapy. Am. J. Roentgenology **72**: 985–988.
2. Cockerham, L. G., Pautler, E. L., Carraway, R. E., Cochrance, D. E. and Hampton, J. D. (1988) Effect of disodium cromoglycate (DSCG) and antihistamines on postirradiation cerebral blood flow and plasma levels of histamine and neurotensin. Fundam. Appl. Toxicol. **10**(2): 233–242.
3. Doyle, T. F. and Strike, T. A. (1977) Radiation-released histamine in the rhesus monkey as modified by mast-cell depletion and antihistamine. Experimentia **33**: 1047–1048.
4. Cockerham, L. G., Doyle, T. F., Pautler, E. L. and Hampton, J. D. (1986) Disodium cromoglycate, a mast cell stabilizer, alters postradiation regional cerebral blood flow in primates. J. Toxicol. Environ. Health **18**: 91–101.
5. Walden, T. L., Jr., and Farzaneh, N. K. (1990) Biochemistry of Ionizing Radiation. Raven Press, New York.
6. Walden, T. L., Jr., and Farzaneh, N. K. (1991) Biochemical responses of normal tissues to ionizing radiation. In "Radiation Injury to the Nervous System". Eds. P. H. Gutin, S. A. Leibel, and G. E. Sheline, pp. 17–36, Raven Press, New York.
7. Cockerham, L. G., Arroyo, C. M. and Hampton, J. D. (1988) Effects of 4-hydroxypyrazolo (3, 4-d) pyrimidine (Allopurinol) on postirradiation cerebral blood flow: Implications of free radical involvement. Free Radic. Biol. Med. **4**(5): 279–284.
8. Cockerham, L. G., Prell, G. D., Cerveny, T. J., O'Brien, M. M. and Hampton, J. D. (1991) Effects of aminoguanidine on pre- and postirradiation regional cerebral blood flow and systemic blood pressure in the primate. Agents and Actions **32**: 237–244.
9. Del Maestro, R. F. (1980) An approach to free radicals in medicine and biology. Acta Physiol. Scand. Suppl. **492**: 153–168.
10. Del Maestro, R. F., Thaw, H. H., Bjork, J., Planker, M. and Arfors, K.-E. (1980) Free radicals as mediators of tissue injury. Acta Physiol. Scand. Suppl. **492**: 43–57.
11. Kennedy, A. R., Troll, W. and Little, J. B. (1984) Role of free radicals in the initiation and promotion of radiation transformation in vitro. Carcinogenesis **5**(10): 1213–1218.
12. Hammond, B., Kontos, H. A. and Hess, H. L. (1985) Oxygen radicals in the adult respiratory distress syndrome, in myocardial ischemia and reperfusion injury, and in cerebral vascular damage. Can. J. Physiol. Pharmacol. **63**: 173–187.
13. Konat, G. W. and Wiggins, R. C. (1985) Effect of reactive oxygen species on myelin membrane proteins. J. Neurochem. **45**: 1113–1118.
14. Kontos, H. A. (1985) Oxygen radicals in cerebral vascular injury. Circ. Res. **57**(4): 508–516.
15. McCord, J. M. (1985) Oxygen-derived free radicals in postischemic tissue injury. New England J. Med.

312(3): 159–163.
16. Carmichael, A. J., Arroyo, C. M. and Cockerham, L. G. (1988) Reaction of disodium cromoglycate (DSCG) with hydrated electrons. Free Radic. Biol. Med. **4**(4): 215–218.
17. Vanhoutte, P. M. (1986) Serotonin, adrenergic nerves, endothelial cells and vascular smooth muscle. Prog. Appl. Microcirc. **10**: 1–11.
18. Reneman, R. S. and Bollinger, A. (1986) Vascular and microvascular effects of serotonin-Some conclusive remarks. Prog. Appl. Microcirc. **10**: 83–86.
19. Hollenberg, N. K. (1988) Serotonin and vascular responses. Ann. Rev. Pharmacol. Toxicol. **28**: 41–59.
20. Rioux, F., Kerouac, R. and St-Pierre, S. (1985) Release of mast cell mediators, vasoconstriction and edema in the isolated, perfused head of the rat following intracarotid infusion of neurotensin. Neuropeptides **6**: 1–12.
21. Suzuki, R., Yamaguchi, T., Li, C-L. and Klatzo, I. (1983) The effects of 5-minutes ischemia in mongolian gerbils: II. Changes of spontaneous neuronal activity in cerebral cortex and CA1 sector of hippocampus. Acta Neuropathol. **60**: 217–222.
22. Kirino, T. and Sano, K. (1984) Selective vulnerability in the gerbil hippocampus following ischemia. Acta Neuropathol. **62**: 201–208.
23. Tolliver, J. M. and Pellmar, T. C. (1987) Ionizing radiation alters neuronal excitability in hippocampal slices of the guinea pig. Radiat. Res. **112**: 555–563.
24. Hollinden, G. E. and Pellmar, T. C. (1989) Attenuation of synaptic trasmission in hippocampal slices following whole animal exposure to ionizing radiation. Soc. Neurosci. Abstr. **15**: 134.
25. Pellmar, T. C., Schauer, D. A. and Zeman, G. H. (1990) Time- and dose-dependent changes in neuronal activity produced by X radiation in brain slices. Radiat. Res. **122**: 209–214.
26. AAPM Task Group 21 (1983) A protocol for the determination of absorbed dose from high-energy photon and electron beams. Med. Phys. **10**: 741–771.
27. Shapiro, S. S. and Wilk, M. B. (1965) An analysis of variance test for normality. Biometrika **52**: 591–611.
28. Remington, R. D. and Schork, M. A. (1970) "Statistics with Applications to The Biological and Health Sciences", pp. 313–315, Prentice-Hall, Inc., Englewood Cliffs, New Jersey.
29. Champman, P. H. and Young, R. J. (1968) Effect of cobalt-60 gamma irradiation on blood pressure and cerebral blood flow in the Macaca mulatta. Radiat. Res. **35**: 78–85.
30. Doyle, T. F., Curran, C. R. and Turns, J. E. (1974) The prevention of radiation-induced, early transient incapacitation of monkeys by an antihistamine. Proc. Soc. Exper. Biol. Med. **145**: 1018–1024.
31. Farrar, J. K., Gamache, F. W., Jr., Ferguson, G. G., Barker, J., Varkey, G. P. and Drake, C. G. (1981) Effects of profound hypotension on cerebral blood flow during surgery for intracranial aneurysms. J. Neurosurg. **55**: 857–864.
32. Taylor, K. M., Gfeller, E. and Snyder, S. H. (1972) Regional localization of histamine and histidine in the brain of the rhesus monkey. Brain Res. **41**: 171–179.
33. Edvinsson, L., Cervos-Navarro, J., Larsson, L. -I., Owman, C. H. and Ronnberg, A. -L. (1977) Regional distribution of mast cells containing histamine, dopamine, or 5-hydroxytryptamine in the mammalian brain. Neurology **27**: 878–883.
34. Gross, P. M. (1982) Cerebral histamine: Indications for neuronal and vascular regulation. J. Cereb. Blood Flow Metabol. **2**: 3–-23.
35. Shenkin, H. A. (1951) Effects of various drugs upon cerebral circulation and metabolism of man. J. Appl. Physiol. **3**: 465–471.
36. Alman, R. W., Rosenberg, M. and Fazekas, J. F. (1952) Effects of histamine on cerebral hemodynamics and metabolism. A. M. A. Arch. Neurol. Psychiat. **67**: 354–356.
37. Krabbe, A. A. and Olesen, J. (1982) Effect of histamine on regional cerebral blood flow in man. Cephalagia **2**: 15–18.
38. Wiggins, R. C., Glatfelter, A., Campbell, A. M., Kunkel, R. C. and Ulevitch, R. J. (1985) Acute

hypotension due to platelet serotonin-induced chemoreflexes after intravenous injection of dextran sulfate in the rabbit. Circ. Res. **57**: 262–277.

39. Freed, C. R., Echizen, H. and Bhaskaran, D. (1985) Brain serotonin and blood pressure regulation: Studies using *in vivo* electrochemistry and direct tissue assay. Life Sciences **37**: 1783–1793.
40. Franzen, F., Gross, H., and Thielicke, G. (1963) Biogene amine in urin und blut von ratten nach subletaler ganzkörperbestrahlung. Strahlentherapie **120**: 598–610.
41. Edvinsson, L. and Owman, Ch. (1976) Amine receptors in brain vessels. In "The Cerebral Vessel Wall". Eds. J. Cervós-Navarro, *et al*, pp. 197–206, Raven Press, New York.
42. Peroutka, S. J. (1988) 5-Hydroxytryptamine receptor subtypes. Ann. Rev. Neurosci. **11**: 45–60.
43. Hawkins, R. N. and Forcino, C. D. (1988) Effects of radiation on cardiovascular function. Comments Toxicology **2**: 243–252.
44. Parsons, A. A. (1991) 5-HT receptors in human and animal cerebravasculature. Trends Pharmacol. Sci. **12**: 310–315.
45. Saxena, P. R., Bom, A. H. and Verdouw, P. D. (1989) Characterization of 5-hydroxytryptamine receptors in the cranial vasculature. Cephalalgia **9**(Suppl 9): 15–22.
46. Baum, S. J., Anno, G. H., Young, R. W. and Withers, H. R. (1985) Symptomatology of Acute Radiation Effects in Humans after Exposure to Doses of 75 to 4500 Rads (cGy) Free-In-Air. DNA-TR-85-50, Defense Nuclear Agency, Washington, DC.
47. Tuor, U. I., Kondysar, M. H. and Harding, R. K. (1988) Emesis, radiation exposure, and local cerebral blood flow in the ferret. Radiat Res. **114**: 537–549.
48. King, G. L. (1988) Characterization of radiation-induced emesis in the ferret. Radiat. Res. **114**: 599–612.
49. Harding, R. K, Hugenholtz, H., Keaney, M. and Kucharzyk, J. (1985) Discrete lesions of the area postrema abolish radiation-induced emesis in the dog. Neurosci. Lett., **53**: 95–100.
50. Frazer, A., Maayani, S. and Wolfe, B. B. (1990) Subtypes of receptors for serotonin. Ann. Rev. Pharmacol. Toxicol. **30**: 307–348.
51. Priestman, T., Challoner, T., Butcher, M. and Priestman, S. (1988) Control of radiation induced emesis with GR38032F (GR). Proc. Am. Soc. Clin. Oncol. **7**: 281 (Abstr. 1089).
52. Bermudez, J., Boyle, E. A., Miner, W. D., and Sanger, G. J. (1988) The anti-emetic potential of the 5-hydroxytryptamine, receptor antagonist BRL 43694. Br. J. Cancer **58**: 644–650.
53. Hunter, A. E., Prentice, H. G., Pothecary, K., Coumar, A., Collis, C., Upward, J., Murdoch, R., Gandhi, L., Hamon, M., Butler, M. and Wells, J. (1991) Granistron, a selective 5-HT3 receptor antagonist, for the prevention of radiation induced emesis during total body irradiation. Bone Marrow Transplant **7**(6): 439–441.
54. King, G. L. and Landauer, M. R. (1990) Effects of zacopride and BMY25801 (batanopride) on radiation-induced emesis and locomotor behavior in the ferret. J. Pharmacol. Exp. Ther. **253**(3): 1026–1033.
55. Fukuda, T., Setoguchi, M., Inaba, K., Shoji, H. and Tahara, T. (1991) The antiemetic profile of Y-25130, a new selective 5-HT3 receptor antagonist. Eur. J. Pharmacol. **196**(3): 299–305.
56. Sharma, H. S., Dey, P. K and Olsson, Y. (1989) Brain edema, blood-brain barrier permeability and cerebral blood flow changes following intracarotid infusion of serotonin: modification with cyproheptadine and indomethacin. In "Pharmacology of Cerebraln Ischemia 1988". Ed. J. Krieglstein, pp. 317–323, CRC Press, Inc., Boca Raton, Florida.
57. Sharma, H. S., Olsson, Y. and Dey, P. K. (1990) Changes in blood-brain barrier and cerebral blood flow following elevation of circulating serotonin level in anesthetized rats. Brain Res. **517**: 215–223.
58. Endlich, K., Kuhn, R. and Steinhausen, M. (1993) Visualization of serotonin effects on renal vessles of rats. Kidney Int. **43**(2): 314–323.
59. Bing, R. J., Chang, B. L., Santillan, G. and Sato, M. (1983) The effect of 5-hydroxytryptamine and arterial blood withdrawal on cerebral microcirculation in the cat, arterial permeability in the rabbit.

Adv. Exp. Med. Biol. **161**: 327–345.
60. Gunter-Smith, P. J. (1987) Effect of ionizing radiation on gastrointestinal physiology. In "Military Rasdiobiology". Eds. J. J. Conklin and R. I. Walker, pp. 135–151, Academic Press, Inc., New York.
61. Hawkins, R. N. and Cockerham, L. G. (1987) Postirradiation cardiovascular dysfunction. In "Military Radiobiology". Eds. J. J. Conklin and R. I. Walker, pp. 153–163, Academic Press, Inc., New York.
62. Young, R. W. (1987) Acute radiation syndrome. In "Military Radiobiology". Eds. J. J. Conklin and R. I. Walker, pp. 165–190, Academic Press, Inc., New York.
63. Russell, L. B., Fike, J. R., Cann, C. E. and Susskind, C. (1984) Dual energy CT scanning for analysis of brain damage due to X-irradiation. Ann. Biomed. Eng. **12**: 15–28.
64. Ludwig, R., Calvo, W., Kober, B. and Brandeis, W. E. (1987) Effects of local irradiation and i.v. methotrexate on brain morphology in rabbits: early changes. J. Cancer Res. Clin. Oncol. **113**: 235–240.
65. Lo, E. H., Frankel, K. A., Steinberg, G. K., DeLaPaz, R. L. and Fabrikant, J. I. (1992) High-dose single-fraction brain irradiation: MRI, cerebral blood flow, electrophysiological, and histological studies. Int. J. Radiat. Oncol. Biol. Phys. **22**: 47–55.
66. Cockerham, L. G., Mickley, G. A., Walden, T. L., Jr. and Stuart, B. O. (1994) Ionizing radiation. In "Principles and Methods of Toxicology", 3rd Ed. Ed. A. W. Hayes, pp. 447–496, Raven Press, New York.
67. Delattre, J. Y., Shapiro, W. R., Posner, J. B. (1989) Acute effects of low-dose cranial irradiation on regional capillary permeability in experimental brain tumors. J. Neurol. Sci. **90**: 147–153.
68. Horsman, M. R., Chaplin, D. J. and Overgaard, J. (1991) The use of blood flow modifiers to improve the treatment response of solid tumors. Radiother. Oncol. **20**: Suppl 1: 47–52.
69. Gobble, G. T., Seilhan, T. M. and Fike, J. R. (1992) Cerebrovascular response after interstitial irradiation. Radiat. Res. **130**: 236–240.
70. Chaplin, D. J., Durand, R. E. and Olive, P. L. (1986) Acute hypoxia in tumors: implications for modifiers of radiation effects. Int. J. Radiat. Oncol. Biol. Phys. **12**: 1279–1282.
71. Cockerham, L. G., Forcino, C. D., Pellmar, T. C. and Smart, S. W. (1987) Effect of methysergide on postirradiation hypotension and cerebral ischemia. Proceedings of the Cerebral Hypoxia and Stroke Symposium, Budapest, Hungary, August 22–24, 1987.
72. Cockerham, L. G., and Forcino, C. D. (1988) Post-irradiation alterations in cerebral blood flow. In "Terrestrial Space Radiation and It's Biological Effects". Eds. P. McCormack, C. E. Swenberg and H. Büecker, pp. 495–507, Plenum Press, New York.

Journal of Microscopy, Vol. 178, Pt 3, June 1995, pp. 240–250.
Received 1 April 1994; accepted 16 January 1995

Evaluation of triple-band filters for quantitative epifluorescence microscopy

R. J. LOWY
Physiology Department, Armed Forces Radiobiology Research Institute, Bethesda, MD 20889–5603, U.S.A.

Key words. Fluorescence microscopy, multi-wavelength, image processing, FITC, Bodipy, Texas Red, Cascade Blue.

Summary

The performance characteristics of two sets of triple-band epifluorescence filters have been evaluated for use with digitally enhanced fluorescence microscopy. Use of such filters, at most, requires movement of the excitation filter, while the dichroic and emission filters remain fixed, allowing multi-wavelength imaging to be performed on standard microscopes. The dyes appropriate for use with these particular filters include Texas Red (TR), Bodipy (BD), FITC and Cascade Blue (CB), four fluorophores now commonly conjugated to both immunochemical probes and other proteins and lipids of biological interest. Good spectral separation existed for most experimental conditions allowing accurate localization of the different fluorophores during multi-wavelength imaging. Anomalous responses were observed during near-UV excitation at high concentration for some dyes. Scanning spectrofluorometry demonstrated that concentration-dependent spectral shifts occurred, resulting in large increases in near-UV absorbance. Despite the complexity of concentration and dye-interaction effects, quantitative measurements of dye concentration could be made, even in regions of multiple dye co-localization. Therefore, multi-band pass filters are an additional valuable approach for performing quantitative fluorescence microscopic imaging.

Introduction

There is considerable interest in simultaneously labelling live cells and fixed specimens with multiple fluorescent probes to examine a wide range of questions in cell and molecular biology. Combined with use of quantitative fluorescence microscopy methods, potentially the amount, location and/or co-localization of the probe molecules within cells or tissues can be accurately determined providing subcellular spatial maps of cellular function. An exhaustive listing of the utility of this approach is beyond the scope of this paper. Examples of important current uses of multi-wavelength fluorescence imaging includes simultaneous pH and intracellular calcium measurements (Morris, 1990, 1993), fluorescence *in situ* hybridization (FISH) (Nederlof *et al.*, 1989), characterization of mass flow during endocytosis (Dunn & Maxfield, 1990), mechanisms of cell damage (Lemasters *et al.*, 1990) and correlation of cytoskeletal elements with other cell structures (DeBiasio *et al.*, 1987; Waggoner *et al.*, 1989) as well as a myriad of studies using immunochemical staining to demonstrate the subcellular distributions of structural proteins and enzymes. General information on the best ways to implement these micro-spectroscopic approaches continues to be the subject of excellent reviews and books, which are frequently updated due to the rapid changes in the technologies underlying this instrumentation, such as dye chemistry, optics, electronics and computer science (for reviews see Herman & Jacobson, 1989; Waggoner *et al.*, 1989; Foskett & Grinstein, 1990; Bright, 1993b).

It is recognized that a very important aspect of digitally enhanced quantitative video fluorescence microscopy is the means for wavelength selection of both the excitation and the emission light. Important issues include wavelength availability, bandpass width, spectral purity, selection speed and energy throughput (Bright, 1993b). Although a variety of sophisticated electro-optic systems are now available (see reviews), use of interference and/or absorbance filters and dichroic mirrors is still probably the most widely used approach at present, being the least costly method for wavelength selection in microscopy. These optical elements are generally not completely dispensed with even in instruments that incorporate other optical or electro-optical wavelength selection, such as confocal microscopes, but continue to be an integral part of such systems. Particularly for standard wide-field microscopes, the usual approach is to have individual filter sets consisting of excitation and emission band-pass filters and dichroic mirrors, each set being optimized for one dye.

Mechanical devices, such as filter wheels and motorized dichroic mirror sliders, are used to switch between the different filter sets. This approach has the advantage of high transmittance with generally low 'cross-talk' between dyes, but switching can be slow and movement of optical elements can lead to misregistration of the multi-wavelength image data. Automatic devices to move dichroic mirrors and emission filters requires either purchase of the most expensive motorized research-grade microscopes or extensive modifications of more typically configured instruments.

A relatively new aspect of interference filter technology for biomedical microscopy is the availability of band-pass filters and dichroic mirrors with multiple band-pass regions. Epifluorescence filter sets capable of simultaneous or sequential excitation and emission for two, three and even four different spectral regions are now available from several vendors. With these filters either no optical elements (simultaneous multi-wavelength viewing) or only the excitation filters (sequential viewing) need be moved. As the mechanical switching components are simplified, instrument speed and reliability can increase, sources of vibration are minimized, image registration is virtually assured and total instrumentation costs can be reduced. Potential remaining problems are (a) reduced signal due to narrower band-pass regions and lower transmittance and (b) increased signal 'cross-talk', e.g. the appearance in the image of emissions of one dye during excitation of a second dye.

Despite the availability of these filters and the interest in multispectral imaging there have been few reports evaluating the quantitative multi-wavelength performance of epifluorescence systems or of the new multi-band pass filters. The most extensive available reports examining quantitative and qualitative performance of system components have been relative to multi-wavelength imaging using confocal microscopy (Brelji *et al.*, 1993; Mossberg & Ericsson, 1990; Carlsson & Mossberg, 1992; Entwistle & Noble, 1992). This study presents data to evaluate the quantitative characteristics of two commercially available triple-band filter sets used for low-light-level epifluorescence video microscopy quantification of Cascade Blue (CB), Bodipy (BD) and Texas Red (TR). An additional goal of this report is to present an experimental methodology, which should be useful for evaluation of other filter–dye combinations. Some of the results have appeared previously in abstract form (Lowy, 1993).

Methods

Dye selection

The dyes were selected in part because of future experimental needs and because these dyes are currently some of the most widely used to label immuochemical probes (Igs), proteins and lipids of biological interest. Many of these biological molecules are now available labelled with several of these dyes, allowing experiments using various combinations of these and other fluorescence probes to examine complex biological interactions of multiple molecular components. The form of the dyes to be used was carefully considered, particularly as it is well known that dye environment can have a large effect on both the magnitude of the excitation and the emission spectra and their shape (Lakowicz, 1983). Therefore, forms of the dyes which required either non-biological solvents or detergents were rejected in favour of forms which would be soluble in normal physiological saline. Protein conjugates were the only available forms of the dyes which fulfilled this solubility criterion for all the fluorophores of interest. However, conjugation can alter dye characteristics either directly or by other protein–molecular interactions. Manufacturer's data suggested that there was little spectral alteration due to linkage, which was confirmed for low dye concentrations (see below). Because of the potential for intramolecular interactions, dye–protein conjugates were considered to be more informative than free dyes as many actual biological probes are proteins. BSA (bovine serum albumin) conjugates, when these studies were conducted, were the only ones available for all four dyes. BSA remains one of the least expensive, most readily available and most diversely labelled dye–protein conjugate. To minimize any dye–protein effects vs. dye interactions, solutions were made with a total BSA concentration of 5 mg/ml, except a few samples in which concentrations were 10 mg/ml.

Dye solutions

Solutions of BSA conjugated with CB, BD or TR (Molecular Probes, Eugene, OR, U.S.A.) were prepared as 10 mg/ml stock solutions in Hanks Basic Saline (HBS), pH 7·4. Dyes were diluted in HBS to the desired dye concentration keeping the protein concentration constant at 5 mg/ml BSA by the addition of unlabelled protein. The dye concentrations are expressed as mg/ml of dye-conjugated BSA; the molar concentrations of dye vary by a factor of approximately 3 as the dye/BSA molar ratios reported by the manufacturer for the various dyes are 2·2 for TR, 5·4 for BD, 5·7 for FITC and 5·5 for CB

Microscopy

Small aliquots of dyes were placed in a Dvorak chamber with spacers and double coverslips such that the dye drop formed a small column 200 μm high, thus providing a constant dye pathlength for all samples. A Nikon 40× 1·3-NA high-UV transmittance lens was focused such that an image of the epifluorescence field diaphragm was formed.

Emission light was detected using a KRS 1381 image intensifier (Videoscope International, Dulles, VA, U.S.A.) optically coupled to a Dage 72C charge coupled device (CCD) (Dage, Michigan City, IN, U.S.A.). Images were captured by an image processing system with 64 frames of integration and the intensity measured at the same central location for all samples.

Spectroscopy

Spectra were obtained using an SLM 8000 (Urbana, IL, U.S.A.) scanning spectrofluorimeter. Slit widths, of 4 or 8 nm, PMT voltages and gain settings were identical for excitation and emission spectra obtained for the individual dyes.

Dye quantification

The image processing system uses 8-bit data (256 grey levels) and the region of interest consisted of approximately 2000 pixels. Camera system gain settings were held relatively constant and all acquisitions were within the linear portion of the camera response curves. These measurement conditions have been shown to give accurate photometric measurements (Spring & Lowy, 1989). The dye intensity was measured in grey levels, but to normalize the data for differing intensifier gain settings appropriate factors were applied to express the data at maximum gain and without neutral density filters. Cross-talk was determined by measuring the emission for each dye singly at all the available excitation wavelengths (360, 490, 560 nm) with values obtained at the dye's excitation maximum set to 100%. For example, the Texas Red cross-talk into Cascade Blue would be calculated as: percentage cross-talk at 360 nm = (Texas Red emission at 360 nm excitation/Texas Red emission at 560 nm excitation maximum) × 100%. The multi-dye experiments were performed by measuring the emission from solutions of each dye singly and then dye mixtures of two or three dyes together at all three excitation wavelengths in succession. The cross-talk corrections were applied where relevant. The resulting value was then compared as a percentage of the single dye, with 100% being the target value.

Filters

The filter sets had excitation and emission band-pass regions corresponding to the reported maximum for Cascade Blue (376, 399ex/423em), Bodipy (505–510ex/520em) and Texas Red (596ex/615em) (Haugland, 1992). One set was commercially available ('Chroma 82000') and was originally produced for FISH studies and therefore had not been optimized for these dyes, but had band-pass regions which nearly matched (Fig. 1). The second set, 85000, based on preliminary results with the 82000 set, was produced to match the dye's spectra better, particularly Cascade Blue. Both sets were designed and manufactured by Chroma Technology, Inc., Brattleboro, VT, U.S.A.

Results

Filters

Figure 1 shows the manufacturer's data for the transmission characteristics of the two filter sets, which have been verified by spectroscopic scanning of selected filters. Both filter sets have relatively high transmittance values for both excitation and emission wavelengths as the 70–80% values are comparable to those reported for single dye epifluorescence filters. As discussed below, in reference to Figs. 4 and 5, the band-pass regions correspond well to the generally reported peak absorption and emission regions of these dyes. Therefore, the limitation on energy throughput for any given band region is the necessary narrowing to minimize spectral overlaps. The 85000 set was expected to perform better with all the dyes, as the triple-band emission filter had broader band-pass regions, but particularly with

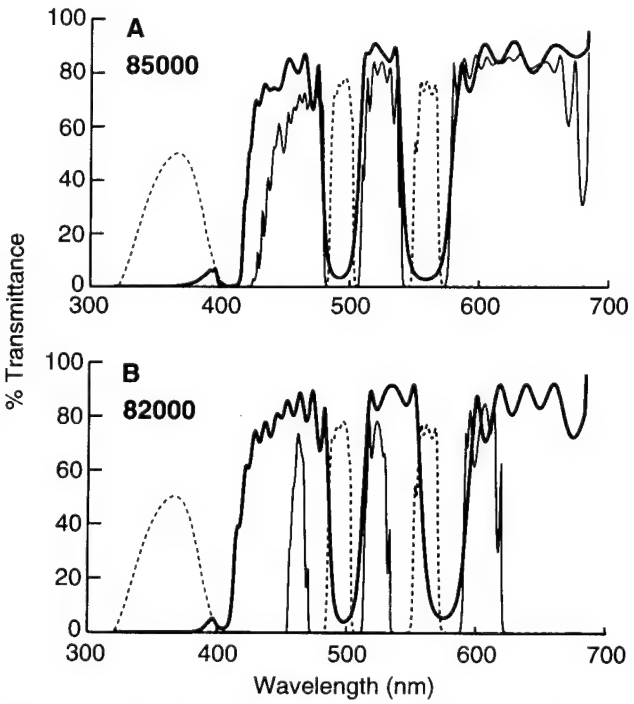

Fig. 1. Spectra of optical transmission vs. wavelength for multi-band filters. (A) The 85000 filter indicated as: emission filter – light solid line; dichroic mirror – heavy solid line; excitation regions – dotted line. (B) The Chroma 82000 filters indicated as: emission filter – light solid line; dichroic mirror – heavy solid line; excitation regions – dotted line. Both filter sets have an emission transmittance of 75% or better, but the 85000 set has wider band-pass regions for all dyes of interest.

Cascade blue, as there was greatest increase in overlap with the dichroic transmission in comparison to the 82000 set. The 'cost' for these greater band widths was that, at present, only sequential excitation of the dyes was possible using the 85000 set, while for the 82000 set a triple-band excitation filter is available, as well as the individual excitation filters.

Detection limits and concentration linearity

Figure 2 shows the fluorescence emission levels vs. concentration for each dye using both filter sets. Data are plotted as log–log to allow the full range of values to be displayed on a single plot. Values over limited ranges of response were examined and in general these relationships were linear over concentration differences of 1000-fold, especially between 1 μg/ml and 1 mg/ml. For the higher concentrations the dyes differed as TR, continuing to show similar proportional increases in emission, but the lines showed some flattening for CB and FITC. Bodipy had a non-linear response over most concentration ranges and at higher concentrations showed little additional increase in fluorescence emission. The data shown are representative but several sets of dilutions were tested with the same result. The fluorescence with the 85000 filters was consistently higher than with the 82000 filters as expected due to greater bandwidths, with the greatest difference occurring at low CB concentrations where a 5–10-fold difference was observed (note log scale). The detection limits for the dyes were between 0·5 and 1 μg/ml, as the fluorescence intensity units scale of approximately 5–10 corresponds to the absolute detection limit of the low-light-level camera system with values of 10–50 probably being a more realistic practical limit with cells due to the increased signal-to-noise ratio. As the pathlength was 200 μm, the actual dye concentration limits for a volume staining of most cells would be 20–40-fold higher, i.e. 10–40 μg/ml.

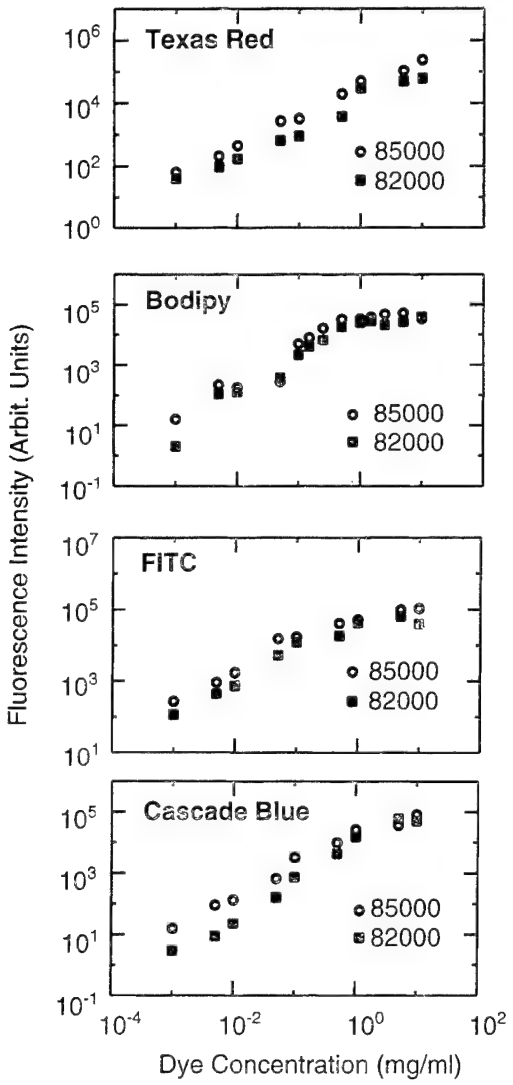

Fig. 2. Single dye emission vs. dye concentration. The emission intensity for TR, BD, FITC and CB were measured using both filter sets for concentrations of dye-BSA between 1 μg/ml and 10 mg/ml. Note the log–log scale. In most cases the relationship is linear over the majority of the concentration range. Detection limits are generally 1–10 μg/ml of dye.

Cross-contamination of dye signals – single dye test

Figure 3 shows the cross-over values for each dye at varying dye concentrations for both filter sets. In each panel the results for the two excitation wavelengths which are not optimal for the particular dye are shown; the value for optimal excitation wavelength is always 100% (see Methods). Another way of considering these cross-over coefficients is that they are the percentage of the maximum emission of the second dye which will be contaminating the dye of interest. In most cases the values are less than 10% and in many instances 5% or less, regardless of dye concentration or the filter set. These results suggest that for most dye–wavelength combinations little or no correction need be done for accurate assessment of either the images or the quantitative values, including areas of dye co-localization. The major exception to this conclusion was for BD, which showed considerable emission when excited at 360 nm, the optimum wavelength for CB. In this case the cross-talk can be very high, up to 40–50% of the emission for 490-nm BD excitation, and shows a very non-linear concentration dependence. Below 0·5 mg/ml with the 85000 filter the percentage is just within acceptable limits.

Cross-contamination of dye signals – multi-dye test

Table 1 presents the results from measuring the emission levels, using the 85000 filter set, for samples prepared combining all the dyes or combinations of two dyes

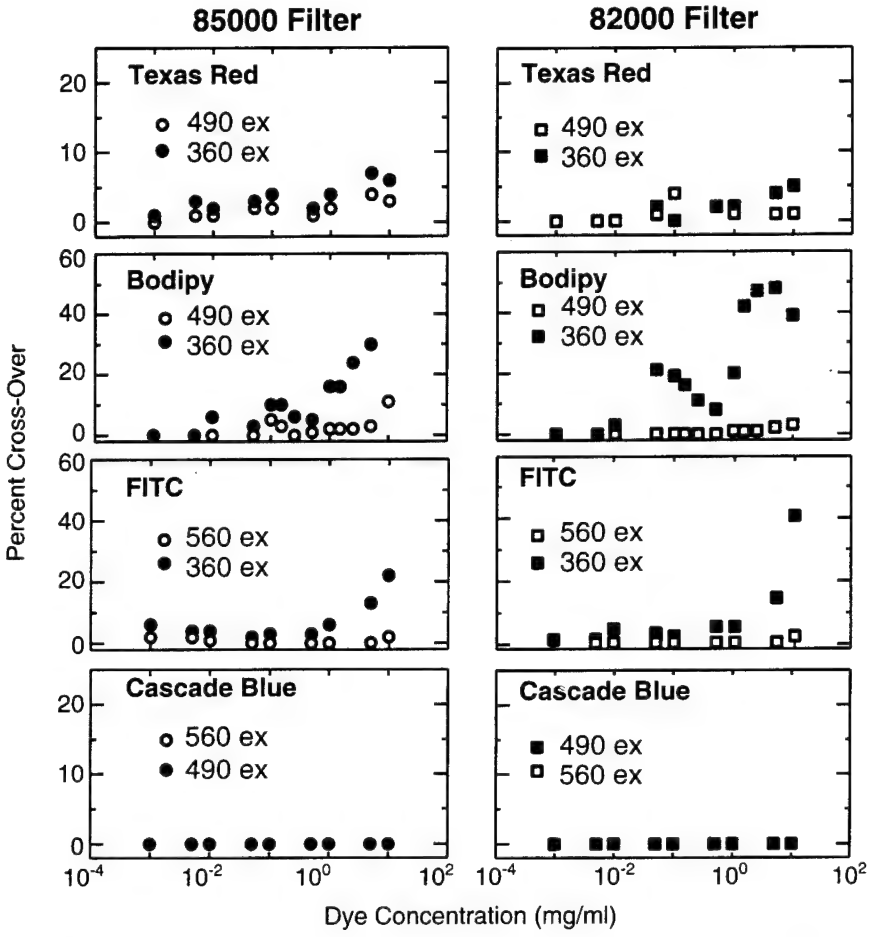

Fig. 3. Filter cross-talk characteristics with single dyes. Cross-talk for dye concentrations between 1 μg/ml and 10 mg/ml were measured for both the 85000 (left panels) and 82000 (right panels) filters for TR, BD, FITC and CB. Values for both non-optimum wavelengths are presented in each panel. The values are the percentage emission for each dye that is excited by wavelengths other than the optimum for that dye normalized to the dye's reported excitation maximum. For Texas Red the optimum excitation filter was 560 nm and the two non-optimum wavelengths are 360 and 490 nm. For most dye, filter and wavelength combinations, cross-talk is less than 10% of the maximal emission obtained at the dye's excitation maximum. BD and FITC at 360 nm and at high concentrations showed much higher levels.

together. As the emission at each wavelength was expressed as a percentage of the single dye value, the expected value in all cases is 100%. Larger values occur when more emission light was observed for a particular dye at its wavelength excitation maximum than expected, while the values of less than 100% indicate the converse. Many values were close to 100% and most were within 20–30% of the target value. The major exceptions were for TR and CB at low concentration, which had values approximately 60% higher than anticipated.

Imaging results

Figure 4 shows the images of the same group of 4·9-μm-

Table 1. 85000 Filter Set Characteristics with Multiple Dye Specimens

	85000 Filter Set Characteristics with Multiple Dye Specimens					
Dye concentration:	1·0 mg/ml			0·1 mg/ml		
Dye:	TR	BD	CB	TR	BD	CB
Dye combination:	Emission detected as percentage of single dye value					
TR + BD + CD	95 ± 2	105 ± 6	108 ± 12	159 ± 20	104 ± 7	163 ± 17
TR + BD	69 ± 2	117 ± 8		100 ± 15	106 ± 7	
TR + CB	100 ± 3		109 ± 11	123 ± 15		107 ± 7
BD + CB		93 ± 6	83 ± 12		78 ± 6	96 ± 6

TR = Texas Red, BD = Bodipy, CB = Cascade Blue. Data are mean ± SEM of six replicate determinations.

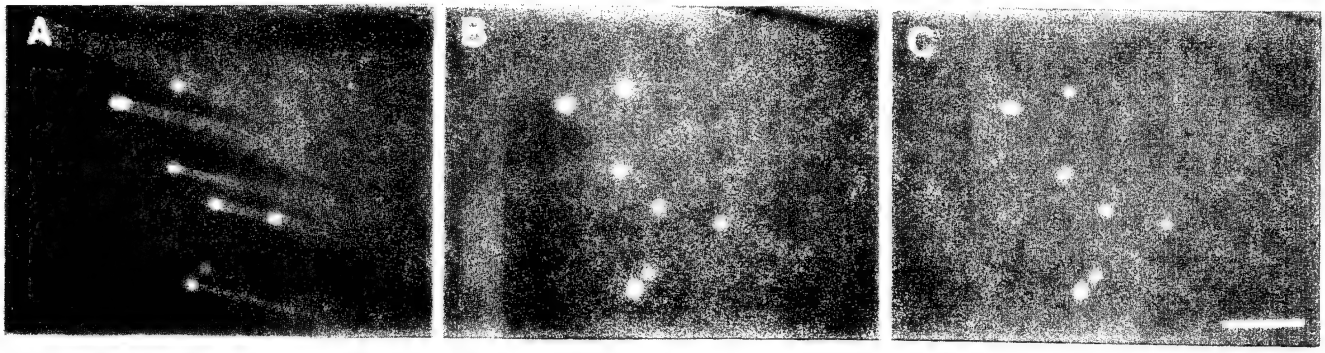

Fig. 4. Polychromatic bead position. Polychromatic beads (4·9-μm diameter, Polyscience, Warrenton, PA, U.S.A) were mounted in glycerol and allowed to settle on a slide which was left undisturbed for 15 min on the microscope stage. Sequential images using the 85000 filter set were acquired for each excitation wavelength (A, 560 nm; B, 490 nm; C, 360 nm). The edges of the photographs are the actual edges of the image processor's display area. The beads show no shifts in position, an important requirement for multiple-wavelength image analysis of probe localization. Scale bar = 20 μm.

diameter polychromatic beads excited at each of the three wavelengths. The positions show no apparent change, as expected, even when examined with further digital enlargement (data not shown).

Figure 5 illustrates the use of these filters for mapping the distribution of two similar intracellular markers either singly or simultaneously. J774 cells were pulse-chased (60/60 min) with only Texas-Red-labelled dextran (TR-Dex; Fig. 5A,B), FITC-labelled dextran (FITC-Dex; Fig. 5C,D) or first with TR-Dex followed by a second pulse chase with FITC-Dex. Cells were examined using all three excitation wavelengths. The labelling was a typical late endosomal and lysosomal labelling pattern, including bright perinuclear compartments, as expected from this pulse-chase protocol. Consistent with the dye cross-talk data (Fig. 3), no cell images were observed at 360 nm excitation (data not shown) nor for single-dye-labelled cells at the non-optimal excitation wavelengths (Fig. 5B,C). Images of double-labelled cells allowed identification of compartments containing both dyes (the majority) as well as clear distinction of those containing a single dye. This identification of double- and singly labelled endosomes or differential levels of labelling could be made despite the close proximity of vesicles of a different type or varying levels of background for the two excitation wavelengths. This was not surprising, as the cross-talk values for TR and FITC were 5% and less than 1%, respectively (Fig. 3).

The band-pass regions for the 85000 filter includes spectral regions which potentially can be used for other commonly used dyes, especially as it is similar to the 82000 filter, which was designed for FISH studies. Figure 6 shows the result of imaging a chromosome spread double-labelled with DAPI and a Texas-Red-labelled antibody to the chromosome's centromere. Clear DAPI-stained images of the spread chromosomes are observed by excitation with the CB filter, while switching to TR excitation allows visualization of the centromeres, with no interference from the chromosome images. The quality of the spectral separation can also be seen with the intraphase nuclei, which appear as bright, diffuse DAPI staining, but the centromeres are clearly visible with 560-nm excitation. Results with the 82000 filter designed for this application were similar, but the intensity values were 4–5 times dimmer (data not shown).

Fluorescence spectroscopy of the dyes

The quantitative results in Figs. 2 and 3 and Table 1 suggested that there are problems in using BD, as the concentration response, cross-over values and the multi-dye sample percentages were particularly anomalous when this dye was present. As in several cases these results showed a concentration dependence, spectral scans of both the excitation and emission spectra were done for BD, CB and TR. It is well known that concentration, like many other physical–chemical parameters in the dye's local environment, can affect the intensity and shape of the spectra. Figures 7 and 8 show the excitation and emission spectra, respectively, for the three dyes, and the three appropriate band-pass regions corresponding to the half-maximum of the 85000 filter set. At low concentration both the excitation and the emission spectra correspond well to those previously reported for these dyes (Mossberg & Ericsson, 1990; Haugland, 1992; Bright, 1993b). However, for all three dyes there is a concentration-dependent shape change in the excitation spectra resulting in a blue shift. This shift for BD and TR is particularly significant as it results in a large increase in the relative amount of absorption in the 300–400-nm region relative to the normal position of the absorption maxima. Excitation at these shorter wavelengths did result in typical emission spectra for all three dyes, as illustrated by the 490- and

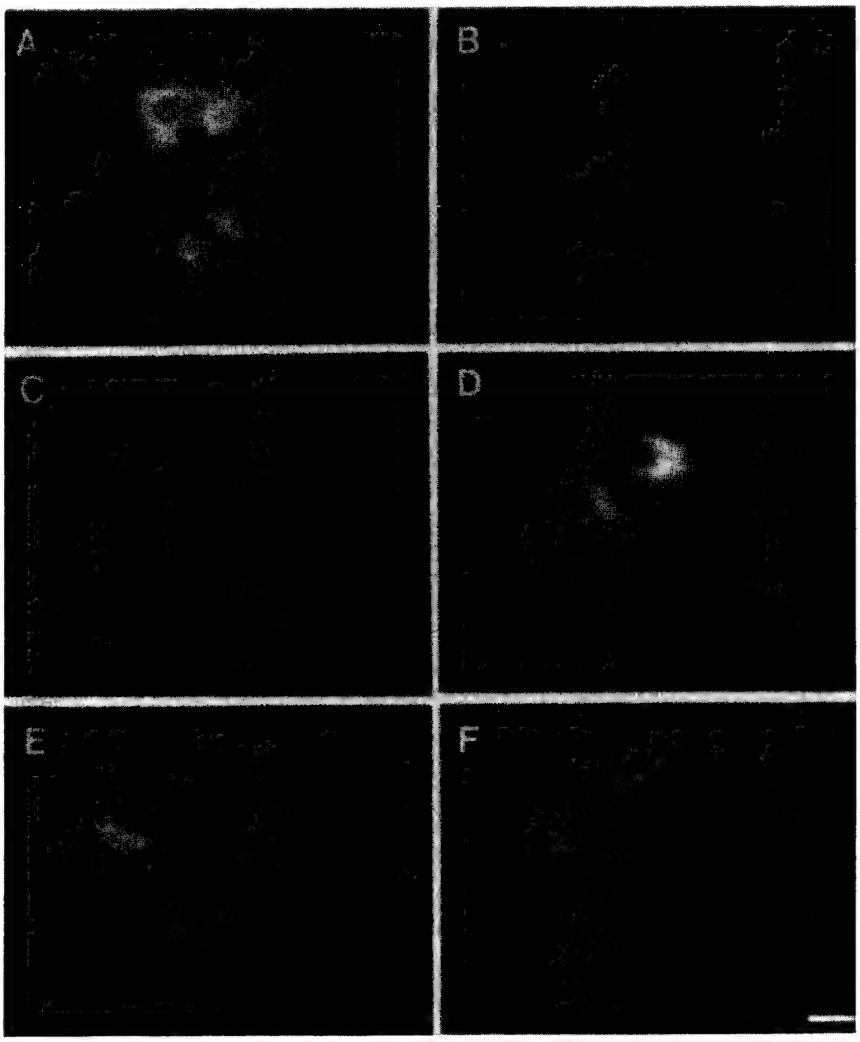

Fig. 5. (A,B) J774.1 cells, a murine macrophage-like cell line, were pulse-chased 60–60 min with TR-Dex (1 mg/ml, 70 kDa) to label late endosomes and lysosomes. (C,D) Cells were pulse-chased 60–60 min with FITC-Dex (1 mg/ml, 70 kDa). (E,F) Cells were first pulse-chased with TR-Dex and then with FITC-Dex. Cells were examined using the 85000 filter set with 560-nm (A,C,E) or with 490-nm (B,D,F) excitation light. No cross-over images are visible in (B) or (C). For double-labelled cells the filter allows clear identification of endosomes with double or single labelling despite varying intensity levels. Scale bar = 20 μm.

360-nm spectra for BD (Fig. 8; other dye data not shown). The concentration dependence of the emissions for any two excitation wavelengths was, of course, dependent on the type of spectra shift occurring. For BD this results in the expected increasing relationship at 360 nm but reversal of the 490-nm values between 0·05 and 0·5 mg/ml of dye. Importantly, these shifts explain the high cross-over results at 360 nm and high concentrations of BD. The calculated ratio is of a decreasing signal at 490 nm combined with an increasing one at 360 nm. The spectroscopic results suggest that this ratio should actually be greater than 100%. However, even using the high-UV transmittance CV lens the photometrically measured amount of 360-nm light is approximately 10 times lower than for 490 nm.

Discussion

The results obtained by evaluating the triple-band filters show that they can be used for quantitative microscopy during multi-spectral imaging, in addition to more qualitative applications. Spectral purity is one of the most important considerations for quantitative multi-wavelength imaging, as lack of wavelength separation when multiple fluorophores are present can make unequivocal interpretation of the images difficult or impossible and can invalidate intensity measurements. The contamination of rhodamine images with emission from fluorescein during dual immunochemical labelling is a common example. During image quantification this can result in an incorrectly higher signal in regions where the dyes co-localize relative to regions where a single dye is present. Importantly, this study demonstrates that the cross-talk is sufficiently low, in most cases, that little or no correction of images is necessary for accurately interpreting the subcellular position of each dye's localization. Studies which require absolute assurance that low signals in a particular image region are not due to low levels of cross-talk could readily be corrected using techniques which are similar to those approaches used in fluorescence-activated cell sorting (Loken *et al.*, 1977) and have been applied to dual-wavelength confocal microscopy

Fig. 6. Metaphase chromosome spreads of human CGL1 cells were counterstained with DAPI. Centromeric sequences were labelled by *in situ* hybridization using a biotin-labelled p824 probe and detected by avidin–Texas Red. Amplification of the Texas Red signal was done by using three cycles. As expected, the DAPI can be seen using the Cascade Blue excitation band-pass regions and does not appear in the Texas Red image of the centromeres. Similar results were obtained with the 82000 filter set, but the image intensity was 2–4 times dimmer. Scale bar = 20 μm.

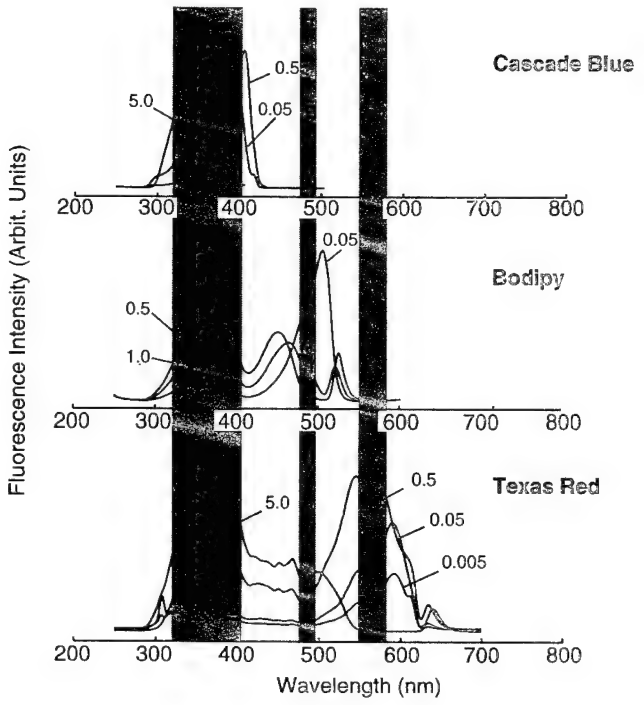

Fig. 7. Excitation spectra are shown for Cascade Blue (top), Bodipy (middle) and Texas Red (bottom). Spectra for several concentrations of dye (0·005–5 mg/ml) are shown and indicated by numbers on spectra in mg/ml. Spectra were not normalized, but obtained with identical instrument settings. Emission wavelengths monitored during scans were 417, 515 and 615 nm for Cascade Blue, Bodipy and Texas Red, respectively. The shaded regions indicate the half-maximum band width for the 85000 excitation filters. All three dyes show spectra shifts and shape changes, which at the higher concentrations alter the amount of dye absorption within the relevant excitation filter band-pass region.

(Carlsson & Mossberg, 1992) and dual pH and calcium imaging (Morris, 1993). The cross-talk percentage values determined here are, like all such values, system dependent, but do provide a guide to the likely magnitude of correction coefficients for several different dyes over a wide range of concentrations. Furthermore, these filters' transmittance is sufficiently high that, by using intensified camera systems, dye concentrations in the low μg/ml range can be readily detected. As expected, movement of the excitation filters did not result in detectable shifts in the apparent position of objects. Therefore, these new filters allow a simplification of the mechanics and reduction in the expense of microscope instrumentation, while still allowing multi-spectral quantitative microscopic image analysis.

An important limitation to multi-spectral imaging may not be the ability to construct filters appropriate for a given combination of dyes, but the behaviour of the dyes themselves. That fluorescence dye spectral properties are frequently greatly affected by the local environment (e.g. solution ionic composition, hydrophobicity, pH and viscosity) is a well known phenomenon (Lakowicz, 1983; David-Dufilho *et al.*, 1988; Poenie, 1990; Carlsson & Mossberg, 1992). In some instances these properties can be exploited to provide additional information, such as ion-sensitive ratiometric dyes (Moore *et al.*, 1990; Ryan *et al.*, 1990; Morris, 1993; Bright, 1993a), while, in others, such as the red shift observed with intracellular probes, these changes become an additional 'noise' factor (Balaban *et al.*, 1986). Photobleaching is another important parameter for microscopic imaging which can alter the relative response to two different dyes. The simplest case is a differential loss of signal due to dye destruction (Entwistle & Noble, 1992), but spectral shifts can also occur (Carlsson & Mossberg, 1992) or changes in sensitivity to the parameter of interest (Becker & Fay, 1987).

In this study only the effects of dye concentration have been considered. The spectral scan results demonstrate that, at least at high concentrations for these BSA conjugates, large changes in the spectroscopic properties can occur, shifting the dyes from one band-pass region to another. These shifts, as well as the flattening of the concentration

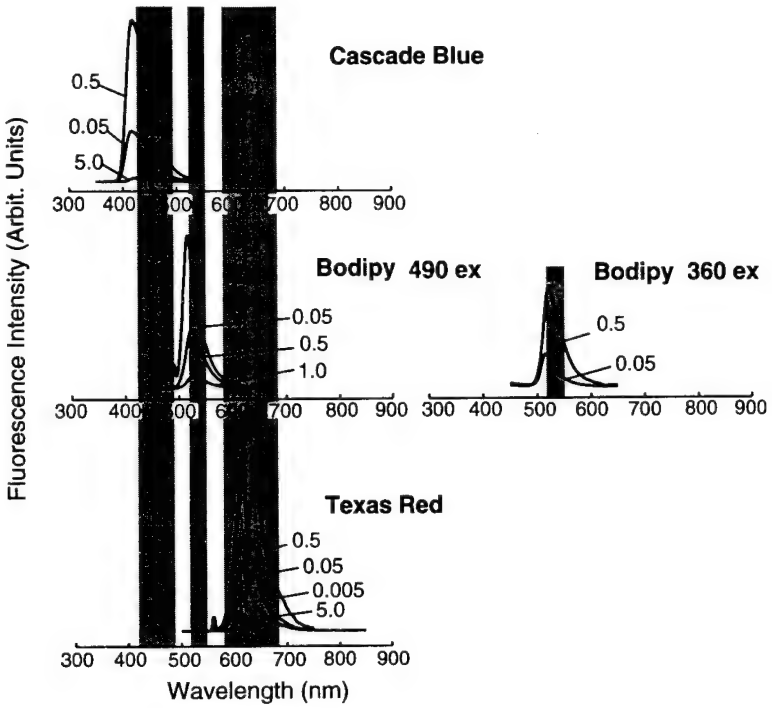

Fig. 8. Emission spectra are shown for Cascade Blue (top) at 360-nm excitation, Bodipy (middle) at 490-nm excitation (left) and 360-nm excitation (right) and Texas Red (bottom) at 560-nm excitation. Spectra for several concentrations of dye (0·005–5 mg/ml) are shown and indicated by numbers on spectra. Spectra are not normalized but obtained with identical instrument settings. The shaded regions indicate the half-maximum band width for the 85000 emission filters. The Bodipy spectra show that both 490- and 360-nm excitation give rise to the same emission centred near 520 nm, the expected wavelength for this dye. The concentration dependence of emission intensity is inverted at 490-nm excitation, which is consistent with the shifts seen in the excitation spectra at these dye concentrations (Fig. 7).

response curves, occurred at dye–BSA conjugate concentrations above 0·5 mg/ml. These effects are unlikely to be due to non-specific dye–unlabelled BSA interactions, as the bulk BSA concentration was constant in all samples, but probably reflect dye–dye interactions. The exact cause of the spectral shifts is at present unclear. There are few reports on dye concentration effects on spectral shape or wavelength shifts, particularly in comparison to studies of solvent effects. The usual concern about high dye concentrations is loss of emission intensity due to inner filter effects, which may also be a factor in this study. Both the decrease in fluorescent emission above 5 mg/ml and a concentration-dependent increase in blue wavelength absorption have been reported for FITC, FITC-Ig and dextran conjugates (Schauenstein *et al.*, 1978). Schauenstein *et al.* (1978) suggested that these shorter wavelength absorptions are due to dimeric forms of the dye. Despite these changes occurring at concentrations which are high for chemical spectroscopy, they are likely to be biologically relevant. While in many biological experiments fluorophore concentrations are in the μg/ml range, in some instances these upper range mg/ml concentrations are used, i.e. injection or exposure of cells to volume markers such as fluorescent dextran. Even if initial levels are low, markers are often used to label specific subcellular compartments, e.g. endosomes, lysosomes and phagosomes, in which the marker concentration becomes elevated. This generally occurs incidentally, but can be an important aspect of the probes utility, such as the red eximer formed during Acridine orange staining (Bank, 1987; Haugland, 1992).

The spectral shifts observed have important implications for the design of both single and multiband-pass filters. Re-examining the fluorescence emission vs. concentration data used to calculate the cross-talk data (Fig. 3) showed that excitation responses of TR, FITC and BD at 360 nm were also linear (data not shown). Therefore, in some circumstances excitation filters and dichroic mirrors which can accommodate the 'tails' on the excitation spectra could provide increased levels of emission light, thus improving sensitivity, assuming that near-UV excitation would not damage the specimen. When designing the band-pass regions for multi-spectral filters and dichroic mirrors for particularly rigorous applications, it will also be necessary to consider these concentration-dependent spectral characteristics, as they can result in decreased sensitivity and/or increased cross-talk.

Immunochemical localization is an important category of microscopic co-localization using multi-wavelenth probes. A calculation was performed to estimate the apparent dye concentration based on the assumption of free in-plane diffusion, a 10-μm-diameter cell, 10 000 dye binding sites, a 1000-mol wt dye, and a 10-nm-thick region surrounding the cell surface. This latter value is based on the relevant volume being a spherical shell with a diameter of the cell and a thickness of the order of 2–3 Ig-sized molecules thick, which are thought to have a size of approximately 4 nm (Alberts *et al.*, 1989). The resulting equivalent free solution concentration is 2 μg/ml. This value can readily be increased to 10 μg/ml by assuming there are 5 dye molecules/Ig. This is near, but not at, the lower limit at which concentration-dependent changes in emission level, cross-talk or spectral shifts were observed. Therefore,

concentration-dependent spectral changes, in general, may be less of a problem for immunochemical localization, but should be considered if either a large number of binding sites exists and/or are in a highly compact region.

In regions in which co-localization of two or three dyes occurs, there are additional considerations in interpreting the quantitative image data. A conservative interpretation of image intensities should take into account the data in Table 1, which suggest that emission from dyes in mixtures may not occur in a truly independent fashion. Emission values should probably differ by 30–50% for dual-wavelength imaging before concluding that there is a significant differential in the local concentration of the two probes. For the triple dye case a value of 60%, or perhaps even a twofold difference, seems warranted. This restriction is not unusually severe in the context of quantitative fluorescence imaging. Considerable important biological information has been obtained with similar constraints from the ion-sensitive ratio dyes, most notably fura-2. Most studies use this dye to examine several-fold changes above the resting cellular level, e.g. changes from 100 to 300–1000 nM, and changes of 20–50% are generally the smallest which can be unequivocally demonstrated accurately (Moore *et al.*, 1990; Roe *et al.*, 1990; Ryan *et al.*, 1990).

In one sense it is surprising that the emission values as measured in the mixtures were not more different from the single dye solutions. The potential complexities of interfilter effects, resonance energy transfer due to the overlapping spectral regions, dye and dye–BSA interactions and different degrees of concentration-dependent absorption spectra shape change all probably contribute to altering the emission magnitude actually observed. Furthermore, the way and degree to which such physical–chemical factors alter fluorescence, as discussed above, is likely to differ for CB, BD and TR, particularly as these are very different classes of organic molecules. For example, with all dyes present, the emission light measured during 360-nm excitation would be expected to be primarily from CB, but possibly with components from TR and BD as well. If we consider only the emission from TR at 360 nm, it can potentially contain components due to direct absorption and resonance energy transferred from both CB and BD directly, as well as energy transferred from CB to BD and finally to TR. The cross-talk term determined from 360-nm excitation of TR alone would correct for the first of these TR components, contributing to an observed CB emission value but not for the resonance effects. The importance of such effects is unknown, and it would require a concerted effort to define these exhaustively for all dye and dye concentration combinations. The data in this study indicate that these effects may be large at low dye concentration and low at high dye concentration, as the CB value was 160 and 109% of the expected value at 0·1 and 1·0 mg/ml, respectively. Nonetheless, considering the complexity of the interactions which could be occurring, it appears that experimentally, even with co-localization of either two or three dyes, reasonably accurate estimates of dye amounts are possible using multi-spectral imaging techniques.

Acknowledgments

The chromosome spread sample with immunostaining was kindly provided by Dr Christopher J. Kolanko of the Armed Forces Radiobiology Research Institute (AFRRI) Biophysics Radiation Department. Valuable discussions with Drs Stephen H. Morris and Gary R. Bright are gratefully acknowledged. The author's work was supported by the AFRRI, Defense Nuclear Agency, under work unit 00020 and NIH/NIAID Grant RO1 AI 35892. Views presented in this paper are those of the author; neither endorsement by the Department of Defense, the Uniform Services University of the Health Sciences or the Armed Forces Radiobiology Research Institute nor other Agency, has been given or should be inferred for any specific product or procedure described. Research was conducted according to the principles enunciated in the Guide for the Care and Use of Laboratory Animals prepared by the Institute of Laboratory Animal Resources, National Research Council.

References

Alberts, B., Bray, D., Lewis, J., Raff, M., Roberts, K. & Watson, J.D., Eds. (1989) *Molecular Biology of the Cell*, 2nd edn. Garland Publishing, Inc., New York.

Balaban, R.S., Kurtz, I., Cascio, H.E. & Smith, P.D. (1986) Microscopic spectral imaging using a video camera. *J. Microsc.* **141**, 131–139.

Bank, H.L. (1987) Rapid assessment of islet viability with acridine orange and propidium iodide. *In Vitro Cell. & Devel. Biol.* **24**, 266.

Becker, P.L. & Fay, F.S. (1987) Photobleaching of fura-2 and its effects on determination of calcium concentrations. *Am. J. Physiol.* **253**, C613–C618.

Brelje, T.C, Wessendorf, M.W. & Sorensen, R.L. (1993) Multicolor laser scanning confocal immunofluorescence microscopy: practical aplications and limitations. *Methods in Cell Biology*, **38**, 97.

Bright, G.R. (1993a) Fluorescence ratio imaging: issues and artifacts. *Optical Microscopy: New Technologies and Applications* (ed. by B. Herman and J. J. Lemasters), pp. 87–114. Academic Press, New York.

Bright, G.R. (1993b) Multiparameter imaging of cellular function. *Fluorescent Probes for Biological Functions of Living Cells – A Practical Guide* (ed. by W. T. Mason and G. Relf), pp. 204–215. Academic Press, New York.

Carlsson, K. & Mossberg, K. (1992) Reduction of cross-talk between fluorescent labels in scanning microscopy. *J. Microsc.* **168**, 23–37.

David-Dufilho, M., Montenay-Garestier, T. & Devynck, M.-A. (1988) Fluorescence measurements of free Ca^{2+} concentration

in human erythrocytes using the Ca^{2+}-indicator fura-2. *Cell. Calcium*, **9**, 167–179.

DeBiasio, R., Bright, G.R., Ernst, L.A., Waggoner, A.S. & Taylor, D.L. (1987) Five-parameter fluorescence imaging: wound healing of living Swiss 3T3 cells. *J. Cell. Biol.* **105**, 1613–1622.

Dunn, K.W. & Maxfield, F.R. (1990) Use of fluorescence microscopy in the study of receptor mediated endocytosis. *Noninvasive Techniques in Cell Biology* (ed. by J. K. Foskett and S. Grinstein), pp. 153–176. Wiley-Liss, New York, NY.

Entwistle, A. & Noble, M. (1992) The use of Lucifer yellow, bodipy, FITC, TRITC, RITC and Texas red for dual immnofluorescence visualized with a confocal scanning laser microscope. *J. Microsc.* **168**, 219–238.

Foskett, J.K. & Grinstein, S., Eds. (1990) *Modern Cell Biology: Noninvasive Techniques in Cell Biology*, Vol. 9. Wiley-Liss, New York.

Haugland, R.P. (ed.) (1992) *Handbook of Flurorescent Probes and Research Chemicals*. Molecular Probes, Inc., Eugene, OR.

Herman, B. & Jacobson, K. (eds) (1989) *Optical Microscopy for Biology*. Wiley-Liss, New York.

Lakowicz, J.R. (ed.) (1983) *Principles of Fluorecence Spectroscopy*. Plenum Press, New York.

Lemasters, J.J., Nieminen, A.-L., Gores, G.J., Dawson, T.L., Wray, B.E., Kawanishi, T., Tanaka, Y., Florine-Casteel, K., Bond, J.M. & Herman, B. (1990) Multiparameter digitized video microscopy (MDVM) of hypoxic cell injury. *Optical Microscopy for Biology* (ed. by B. Herman and K. Jacobson), pp. 523–541. Wiley-Liss, New York.

Loken, M.R., Parks, D.R. & Herzenberg, L.A. (1977) Two-color immunofluorecence using a fluorescence-activated cell sorter. *J. Histochem. Cytochem.* **25**, 899–907.

Lowy, R.J. (1993) Characterization of triple band filter for multi-wavelength epifluorescence video microscopy. *Molec. Biol. Cell Suppl.* **4**, 112a.

Moore, E.D.W., Becker, P.L., Fogarty, K.E., Williams, D.A. & Fay, F.S. (1990) Ca^{2+} imaging in single living cells: Theoretical and practical issues. *Cell. Calcium*, **11**, 157–179.

Morris, S.J. (1990) Real-time multi-wavelength fluorescence imaging of living cells. *Biotechniques*, **8**, 296–308.

Morris, S.J. (1993) Simultaneous multiple detection of fluorescent molecules: rapid kinetic imaging of calcium and pH in living cells. *Optical Microscopy: New Technologies and Applications* (ed. by B. Herman and J. J. Lemasters), pp. 177–212. Academic Press, New York.

Mossber, K. & Ericsson, M. (1990) Detection of doubly stained fluorescent specimens using confocal microscopy. *J. Microsc.* **158**, 215–224.

Nederlof, P.M., Robinson, D., Abuknesha, R., Wiegant, J., Hopman, A.H.N., Tanke, H.J. & Raap, A.K. (1989) Three-color fluorescence in situ hybridization for the simultanous detection of multiple nucleic acid sequences. *Cytometry*. **10**, 20–27.

Poenie, M. (1990) Alteration of intracellular fura-2 fluorescence by viscosity: a simple correction. *Cell. Calcium*, **11**, 85–91.

Roe, M.W., Lemasters, J.J. & Herman, B. (1990) Assessment of fura-2 for measurements of cytosolic free calcium. *Cell. Calcium*, **11**, 63–73.

Ryan, T.A., Millard, P.J. & Webb, W.W. (1990) Imaging [Ca2+]i dynamics during signal transduction. *Cell. Calcium*, **11**, 145–155.

Schauenstein, K., Schauenstein, E. & Wick, G. (1978) Fluorescence properties of free and protein bound fluorescein dyes I. Macrospectrofluorometric measurements. *J. Histochem. Cytochem.* **26**, 277–283.

Spring, K.R. & Lowy, R.J. (1989) Characteristics of low light level television cameras. *Methods. Cell. Biol.* **29**, 269–289.

Waggoner, A., DeBiasio, R., Conrad, P., Bright, G.R., Ernst, L., Ryan, K., Nederlof, M. & Taylor, D. (1989) Multiple sectral parameter imaging. *Methods in Cell Biology: Fluorescence Microscopy of Living Cells in Culture Part B* (ed. by D. L. Taylor and Y. -L. Wang), pp. 449–478. Academic Press, New York.

ELSEVIER

Journal of Neuroscience Methods 59 (1995) 93–98

JOURNAL OF NEUROSCIENCE METHODS

Use of brain slices in the study of free-radical actions

Terry C. Pellmar *

Department of Physiology, Armed Forces Radiobiology Research Institute, 8901 Wisconsin Avenue, Bethesda, MD 20889-5603, USA

Received and accepted 4 November 1994

Abstract

To understand the neuropathological roles of free radicals we investigate their actions in a model neuronal system, the hippocampal brain slice. Free radicals can be generated through a number of methods: hydrogen peroxide to produce hydroxyl radicals, dihydroxyfumarate to generate superoxide and ionizing radiation producing a variety of radical species. We find that free radicals have a number of profound effects in this system, which can be prevented by free-radical scavengers and antioxidants. With exposure to free radicals, the ability to generate spikes and synaptic efficacy are impaired. Decreased spike generating ability is correlated with lipid peroxidation. No change in membrane potential, membrane resistance, or many of the potassium currents can account for the effect on spike generation. Protein oxidation is likely to underlie synaptic damage. Both inhibitory and excitatory synaptic potentials are reduced by free-radical exposure. Presynaptic mechanisms are implicated. Lower concentrations of radicals prevent the maintenance of long-term potentiation, perhaps through oxidation of the NMDA receptor. The actions of the free radicals are often reversible because of the presence of repair mechanisms, such as glutathione, in hippocampal slices. The brain slice preparation has allowed us to begin to understand the electrophysiological and biochemical consequences of free-radical exposure.

Keywords: Hippocampal slice; Free radical; Synaptic transmission; Lipid peroxidation; Peroxide; Superoxide; Hydroxyl radical

1. Introduction

Oxygen free radicals are extremely short-lived reactive species that are implicated in the etiology of many nervous system pathologies such as stroke, Parkinson's disease and amyotrophic lateral sclerosis. To understand the neuropathological roles of free radicals, it is necessary to understand the variety of physiological mechanisms that they can disrupt. An in vitro preparation offers many important characteristics that are essential to this aim. An isolated neural preparation provides a system in which the radicals can be controllably generated through a variety of methods and comparisons of reactive oxygen species can be made by pharmacologically manipulating the neuronal environment. In addition, the complicating factors of alterations of blood flow and ischemic episodes which can themselves generate free radicals are eliminated in the slice preparation. Studies on repair mechanisms are possible because of the capability of chemical modulation of the tissue in a controlled environment. Finally the hippocampal brain slice is an integrated neural network with easily accessible circuitry and functioning glia and neurons. In this preparation, the many different cellular processes subject to free-radical attack can be defined. This report summarizes some of our recent findings characterizing the mechanisms of free-radical damage.

2. Methods

2.1. Slice preparation

The hippocampus was isolated from euthanized guinea pigs and cut into thin slices approximately 425 μm thick. Tissue was incubated at room temperature for at least 1 h in oxygenated (with 95% O_2/5% CO_2) artificial cerebrospinal fluid (ACSF) with the following composition: 124 mM NaCl, 3.0 mM KCl, 2.4 mM $CaCl_2$, 1.3 mM $MgSO_4$, 1.24 mM KH_2PO_4, 10 mM glucose and 26 mM $NaHCO_3$. ACSF was made daily and all drugs were added immediately before use.

* Corresponding author. Tel.: (301) 295-1346; Fax: (301) 295-0313.

Elsevier Science B.V.
SSDI 0165-0270(94)00198-7

2.2. Electrophysiology

Slices were transferred to a submerged-slice chamber where they were perfused at 1–2 ml/min with ACSF warmed to 30°C. A bipolar stimulating electrode was positioned in the stratum radiatum of field CA1. The afferents were activated with constant current stimuli (0.1–1 mA, 200–300 μs). Field potentials were recorded with glass microelectrodes filled with 2 M NaCl. One recording electrode was placed in the stratum radiatum to record the afferent volley and the population postsynaptic potential (PSP). A second electrode was positioned in the stratum pyramidale to record the population spike. Intracellular recordings were obtained from pyramidal cells of field CA1 with sharp electrodes (20–40 MΩ) filled with either 2 M KCl or 3 M potassium acetate. All current clamp and voltage clamp recordings were made with a single-electrode recording amplifier (Axon Instruments or Dagan) with the switching frequency set at 4–6 kHz and a 25% duty cycle. The headstage was continually monitored to ensure accurate adjustment of the capacitance feedback and to watch for changes in electrode characteristics. Potentials were recorded with high-gain amplifiers and digitized, stored and analyzed on a dedicated computer.

2.3. Lipid peroxidation

Lipid peroxidation was measured by the thiobarbituric acid test for malondialdehyde. Hippocampal slices from a single animal were separated into control (untreated) and experimental groups and incubated in the experimental solutions for 30 min. At least 3 slices were required for each group. Tissue was homogenized in 1 ml of 20% trichloracetic acid with 0.5 mM EDTA, followed by the addition of 2 ml of 67% thiobarbituric acid in 20 mM NaOH. The solution was then boiled for 10 min and centrifuged at 2400 rpm for 10 min. Absorbance of the supernatant was measured at 530 nm. Results were standardized by the tissue's wet weight.

2.4. Glutathione measurement

Total tissue glutathione was measured with the Tietze assay. At least 2 slices for each experimental condition were homogenized in 0.12% sulfosalicylic acid/0.2% Triton X-100 and allowed to stand for 10 min or more. The suspension was centrifuged at 12,000 rpm for 4 min and the supernatant combined with dithiobis-nitrobenzoic acid and NADPH. The addition of glutathione reductase produced thionitrobenzoic acid, which was monitored at 412 nm.

To reduce tissue glutathione by 20%, slices were incubated with 5 mM buthionine sulfoximine for 2 h before use (Pellmar et al., 1992). Remaining glutathione could be inactivated by exposure to 100 μM dimethylfumarate (DMF), which covalently binds glutathione (Biaglow et al., 1982). Treatment with DMF effectively removed all remaining glutathione from the tissue (Pellmar et al., 1992).

2.5. Generation of free radicals

In an in vitro brain slice preparation, several approaches can be used to generate free radicals. Chemical generating systems (i.e., through Fenton chemistry or auto-oxidation reactions) can produce radicals in the perfusate. Alternatively, ionizing radiation can be used to generate reactive oxygen compounds throughout the neuronal tissue.

2.5.1. Hydrogen peroxide

Hydrogen peroxide reacts with tissue iron to produce the hydroxyl free radical through the Fenton reaction.

$$H_2O_2 + Fe^{+2} \rightarrow OH^{\cdot} + Fe^{+3} + OH^{-}$$

Addition of iron to the ACSF is not necessary to generate hydroxyl radicals; there is sufficient iron in the reagents and in the tissue to allow the Fenton reaction (Pellmar et al., 1989; Myers et al., 1994). Since peroxide is freely permeable through cell membranes, hydroxyl radicals are likely to form wherever iron (or copper) are located, both intracellularly and extracellularly.

The hydroxyl radical reacts with the spin trap DMPO to produce a relatively stable adduct that can be measured with ESR techniques. Hippocampal slices in ACSF show the characteristic 1:2:2:1 pattern after treatment with hydrogen peroxide (Myers et al., 1994). With time, the pattern changes suggesting that carbon-centered radicals are being formed, which is consistent with the physiological damage taking place.

2.5.2 Superoxide radicals

Superoxide radicals were generated through the autoxidation of dihydroxyfumarate (DHF). A concentration of 3 mM was found to be effective in hippocampal slices as well as in other in vitro systems (Barrington et al., 1988; Pellmar and Lepinski, 1992). Dihydroxyfumarate reacts with oxygen to produce superoxide and the oxidation product, diketosuccinate (Halliwell, 1977). With this system, superoxide is generated extracellularly. Although the negatively charged superoxide can enter cells through anion channels, due to the low resting anion permeability of neurons, it is unlikely that these radicals have significant access to the intracellular space in neural tissue.

2.5.3. Ionizing radiation

Ionizing radiation deposits its energy, in part, by generating free radicals in the intracellular and extra-

cellular aqueous environment. A 60-cobalt source was used to provide γ-radiation (Tolliver and Pellmar, 1987). As the slices were cut, they were alternately placed in one of two beakers of oxygenated ACSF. After the incubation period, both beakers were transported through the building to the cobalt facility (3–4 min interval). When there, one of the beakers was positioned in the radiation field while the other beaker was shielded from the radiation source. At least one slice from each beaker was evaluated electrophysiologically to allow comparison of tissue obtained from the same animal.

An alternative method of radiation exposure has been developed in which an X-ray unit is positioned within a lead Faraday cage (Schauer et al., 1989; Pellmar et al., 1990). With this arrangement, we can record from brain slices before and during radiation exposure. The X-ray source was configured with a molybdenum target and filter to generate primarily 17.4 keV photons. Tube current was used to regulate the dose-rate to the tissue at a constant potential and at a constant distance from the slices in the perfusion chamber. Dosimetry was performed on line with a plastic scintillator, calibrated with a parallel-plate ionization chamber. Because the X-rays were minimally penetrating, extra care was taken to ensure that the fluid level above the tissue was constant and minimal.

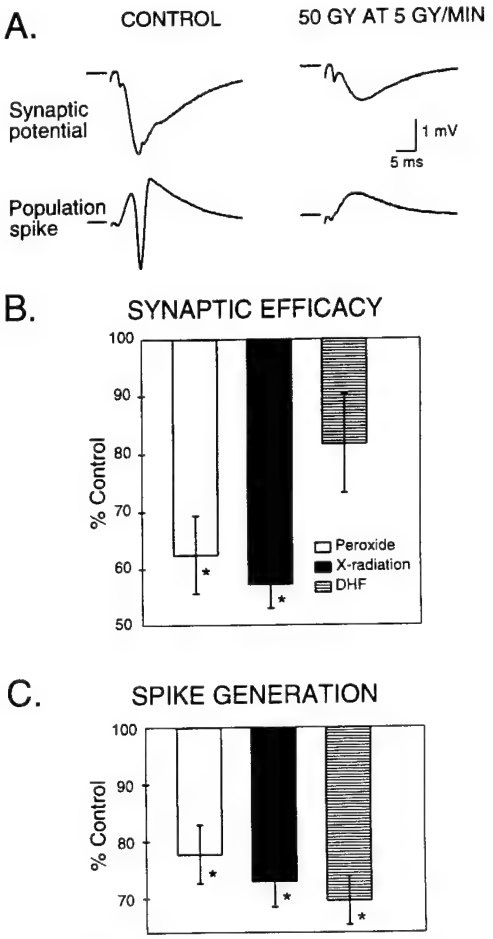

Fig. 1. Synaptic efficacy and spike generation are reduced by free radicals. A: sample field potential recordings obtained from field CA1 of guinea pig hippocampal slice before and after exposure to 50 Gy X-radiation at a dose rate of 5 Gy/min. The synaptic response to stimulation of stratum radiatum was significantly decreased by the radiation. The resulting population spike was completely blocked by the exposure. B: reduction in synaptic efficacy by hydrogen peroxide (3 mM), X-radiation (50 Gy at 5 Gy/min) and dihydroxyfumarate (3 mM). The effects of dihydroxyfumarate were not statistically significant. C: reduction in spike generation by hydrogen peroxide (3 mM), X-radiation (50 Gy at 5 Gy/min) and dihydroxyfumarate (3 mM). The effects reflect the decreased ability of constant size synaptic potential to elicit a population spike. $n = 9$ for peroxide, $n = 4$ for X-radiation, $n = 7$ for dihydroxyfumarate. * reflects significance at $P < 0.05\%$.

3. Results and Discussion

3.1. Electrophysiological effects of free-radical exposure

Peroxide-generated hydroxyl radicals have multiple effects in the hippocampal slice preparation. Two deficits are evident electrophysiologically: a decrease in spike generation and a decrease in synaptic efficacy (Fig. 1). Exposure to 1.0–3.0 mM peroxide caused a decrease in the synaptic potentials recorded both extracellularly and intracellularly. Both excitatory and inhibitory potentials were reduced. In addition, a larger synaptic potential was required to elicit an orthodromic spike. Intracellularly, fewer action potentials were elicited by a depolarizing current step. These effects were reversible when the peroxide was removed from the bathing solution (Pellmar, 1986; Pellmar, 1987).

Antioxidants were able to prevent the consequences of peroxide exposure (Pellmar et al., 1989). Pre-incubation of the hippocampal slice with the iron chelator desferal provides significant protection of both the decrease in synaptic transmission and the decrease in the ability to generate spikes. Since chelation of the available iron would prevent the Fenton reaction (Graf et al., 1984), these results suggest that the hydroxyl radical, and not the peroxide itself, was responsible for the observed effects. Pretreatment with the antioxidant Trolox-C was also capable of mitigating the actions of peroxide. The free-radical scavenger DMSO protected against the decrease in spike generation but not the decrease in synaptic efficacy.

Superoxide, generated from dihydroxyfumarate, only decreased spike generation. Synaptic potentials were not reduced by 3 mM DHF (Fig. 1). The enzyme superoxide dismutase (SOD) catalyzes the reaction converting superoxide to hydrogen peroxide. Catalase can then break down the hydrogen peroxide to water

(Fridovich, 1978; Fridovich, 1983; Halliwell and Gutteridge, 1985). Pretreatment with SOD did not prevent the actions of DHF. On the contrary, when SOD was present, DHF decreased the synaptic potentials as well as spike generation. Pretreatment with both catalase and SOD prevented both effects of DHF. In fact, catalase alone was able to significantly reduce the impairment of spike generation by DHF. These data suggest that the actions of DHF are primarily mediated through spontaneous dismutation of superoxide to hydrogen peroxide and this process was enhanced by the addition of SOD (Pellmar and Lepinski, 1992). As discussed above, hydroxyl radicals are likely to mediate the actions of the DHF-generated peroxide.

Exposure to ionizing radiation at high dose rates ($\geq$ 5 Gy/min) produced changes in hippocampal tissue that resembled those of hydrogen peroxide (Fig. 1). Both the population spike and the synaptic potential were decreased. However, unlike peroxide or DHF exposure, the effects of radiation were not reversible with time after exposure. Both X- and γ-radiation produced similar effects. Higher doses ($\geq$ 75 Gy at 20 Gy/min) were required to observe significant effects with the γ-radiation because comparisons were made between slices from the same animal (Tolliver and Pellmar, 1987). In contrast, X-radiation allowed comparisons within the same slice, and, consequently, there was less variability in the data. The radiation effects on synaptic efficacy showed a strong sensitivity to dose rate. Higher dose-rates were more effective in decreasing synaptic efficacy. In fact, at very low dose-rates, synaptic efficacy significantly increased (Pellmar et al., 1990).

3.2. Recovery from free-radical damage due to repair mechanisms

Glutathione is a non-protein thiol found in high concentrations in most cell types. It is a powerful reducing agent and, through a variety of biochemical pathways, acts to repair oxidation damage (Meister, 1983; Mitchell, 1988; Reed, 1990). Glutathione can be partially depleted by inhibition of its synthesis with buthionine sulfoximine (Griffith and Meister, 1985). Partial depletion to 80% of control levels allowed only partial recovery from peroxide damage. Reaction with dimethyl fumarate completely depleted glutathione in hippocampal slices. This treatment did not enhance the effects of hydrogen peroxide but prevented any recovery from the damage. These data suggest that glutathione is required for repair of free-radical damage in hippocampal slices. It is possible that the glutathione repair system (and/or other repair mechanisms) is inactivated by ionizing radiation preventing the reversal of the damage.

3.3. Mechanisms of spike generation decrease

The ability to generate orthodromic spikes was impaired by all of the free-radical generating systems we have used: hydrogen peroxide, dihydroxyfumarate and ionizing radiation. A larger synaptic potential was required to elicit an orthodromic action potential. In addition, the number and the frequency of action potentials elicited by depolarizing current in a pyramidal cell were reduced by peroxide-generated hydroxyl radicals.

Experimental evidence suggests that the decrease in spike generation is correlated with lipid peroxidation. With free-radical attack of membrane lipids, hydroperoxides are formed in the membrane, and crosslinking between the lipids occurs (Halliwell and Gutteridge, 1985). Hippocampal slices treated with hydrogen peroxide or with DHF demonstrated an increase in lipid peroxidation (Fig. 2). Lipid peroxidation initiated by hydrogen peroxide was prevented by pretreatment with desferal, Trolox-C or DMSO. DHF-induced lipid peroxidation was prevented by pretreatment with SOD plus catalase or by DMSO. The pharmacological sensitivity of lipid peroxidation correlated with the decrease in spike generation but not with the decrease in synaptic efficacy. DHF, which did not alter synaptic transmission, did elicit lipid peroxidation. DMSO did not protect against the peroxide-induced decrease in synaptic efficacy but did prevent both changes in spike generation and lipid peroxidation. In addition, the observation that impairment of spike generation was minimally sensitive to changes in dose-rate further supports a lipid peroxidation mechanism for this electrophysiological effect. Lipid peroxidation is known to show inverse dose-rate sensitivity or limited sensitivity at the higher dose rates of ionizing radiation (Raleigh et al., 1977).

The physiological mechanisms for the decreased ability to generate spikes are still unknown. Intracellular recordings indicated that membrane potential, membrane resistance, membrane capacitance and sodium spike threshold are not measurably changed with exposure to hydrogen peroxide. Voltage clamp recordings of membrane currents isolated pharmacologically demonstrated that none of the tested potassium currents (A, K, C or Q) were altered by free-radical exposure (Pellmar, 1987). It is possible that sodium-current activation kinetics could be altered by free radicals and lipid peroxidation, resulting in decreased spike frequency. This possibility remains to be tested.

3.4. Mechanisms of decreased synaptic efficacy

Oxidation of cellular proteins is likely to mediate the changes in synaptic transmission (Pellmar and Neel,

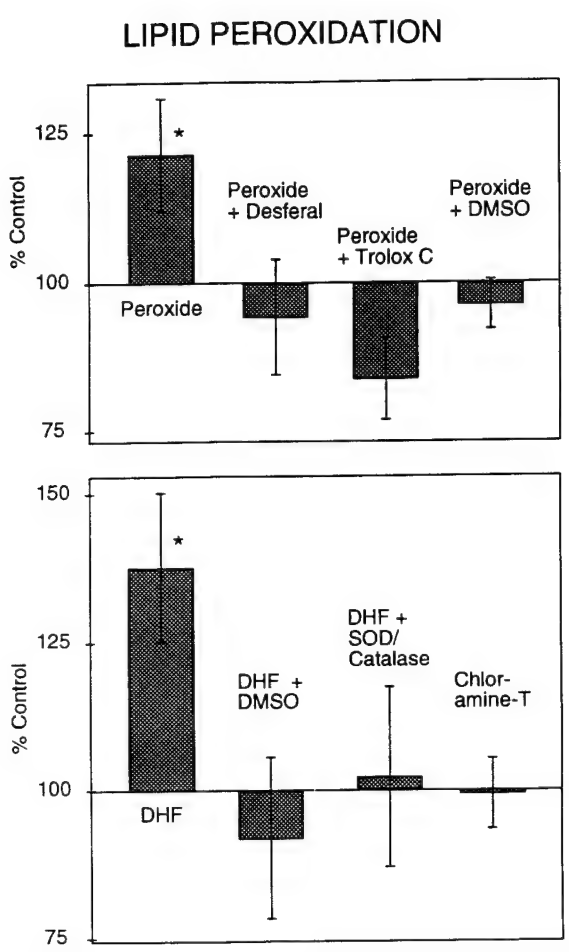

Fig. 2. Lipid peroxidation is elicited by 3 mM hydrogen peroxide and 3 mM dihydroxyfumarate but not by chloramine-T. Desferal, Trolox-C and DMSO prevent the peroxide-induced lipid peroxidation. SOD plus catalase and DMSO prevent the DHF-induced lipid peroxidation. % change was calculated from a ratio of the experimental condition and a paired control. Lipid peroxidation was measured by the thiobarbituric acid assay. $n = 8–10$ for all groups. * reflects significance at $P < 0.05\%$.

1989). Chloramine-T and N-chlorosuccinimide are capable of oxidizing cellular proteins (Schechter et al., 1975). Exposure of hippocampal slices to these agents did not cause lipid peroxidation and did not alter spike generation. However, the oxidizing agents selectively decreased synaptic efficacy.

Presynaptic damage is likely to account for the free-radical induced impairment of synaptic transmission. Although both GABA-mediated inhibitory postsynaptic potentials and glutamate-mediated excitatory postsynaptic potentials were decreased by free-radical exposure, responses to iontophoretically applied neurotransmitter were insensitive. Depolarizing responses to glutamate primarily activated non-NMDA receptors. Responses to GABA near the cell bodies CA1 pyramidal cells were hyperpolarizing, while on the dendrites were depolarizing. None of these responses were affected by high concentrations (3 mM) of hydrogen peroxide. A presynaptic mechanism was postulated (Pellmar, 1986) and supported by subsequent studies showing a decrease of calcium-dependent release of glutamate and of GABA from cerebrocortical synaptosomes (Gilman et al., 1992).

In contrast to non-NMDA, glutamate receptors, postsynaptic NMDA receptors are likely to be vulnerable to free radicals (Aizenman et al., 1990). With oxidation of these receptors, the responses to NMDA are decreased (Aizenman et al., 1989). In the presence of DNQX to block the non-NMDA receptors and low-magnesium-containing ACSF to remove the voltage sensitivity of the NMDA response, orthodromic stimulation of the stratum radiatum produced a synaptic potential that was completely blocked by exposure to APV, an NMDA receptor antagonist. This synaptically evoked NMDA-mediated response was very sensitive to hydrogen peroxide. It was decreased by concentrations (580 μM peroxide) that have no effect on the normal synaptic potential or on presynaptic events. Similar concentrations of hydrogen peroxide prevent the maintenance of long-term potentiation (LTP) in field CA1 of the hippocampus (Pellmar et al., 1991; Colton et al., 1989). Because NMDA receptor activation is necessary for production of LTP in this area of hippocampus, we hypothesize that the oxidation of NMDA receptors by free radicals mediate these actions of hydrogen peroxide.

4. Conclusions

With the use of hippocampal slice preparation, we have started to define the electrophysiological and biochemical consequences of free-radical exposure. Lipid peroxidation of cellular membranes results in a decreased ability of the neurons to generate spikes. Free radicals decrease both inhibitory and excitatory synaptic potentials through a presynaptic mechanism. Oxidation of proteins is likely to underlie the damage. In addition, oxidation of postsynaptic NMDA receptors disrupt neuronal plasticity. Other actions of free radicals, such as a decrease in uptake of glutamate and of GABA (Gilman et al., 1994; Pellmar et al., 1994; Volterra et al., 1994) are also likely to contribute to neurophysiological deficits. With our increasing knowledge, future treatments of free-radical-mediated syndromes can be targeted to vulnerable mechanisms.

Acknowledgements

I thank Kyung Lee, Dennis Lepinski, Larry Myers, Kathryn Neel, Deborah Roney, David Schauer, James Tolliver and Gary Zeman for their valuable contribu-

tions to these studies. Supported by the Armed Forces Radiobiology Research Institute under work unit 00105. Research was conducted according to the principles in the *Guide for the Care and Use of Laboratory Animals* prepared by the Institute of Laboratory Animal Resources, National Research Council.

References

Aizenman, E., Lipton, S.A. and Loring, R.E. (1989) Selective modulation of NMDA responses by reduction and oxidation, Neuron, 2: 1257–1263.

Aizenman, E., Hartnett, K.A. and Reynolds, I.J. (1990) Oxygen free radicals regulate NMDA receptor function via a redox modulatory site, Neuron, 5: 841–846.

Barrington, P.L., Meier, C.F. and Weglicki, W.B. (1988) Abnormal electrical activity induced by free radical generating systems in isolated cardiocytes, J. Mol. Cell. Cardiol., 20: 1163–1178.

Biaglow, J.E., Varnes, M.E., Astor, M. and Hall, E.J. (1982) Nonprotein thiols and cellular response to drugs and radiation, Int. J. Radiat. Oncol. Biol. Phys., 8: 719–723.

Colton, C.A., Fagni, L. and Gilbert, D. (1989) The action of hydrogen peroxide on paired-pulse and long-term potentiation in the hippocampus, Free Radical Biol. Med., 7: 3–8.

Fridovich, I. (1978) The biology of oxygen radicals, Science, 201: 875–880.

Fridovich, I. (1983) Superoxide radical: an endogenous toxicant, Annu. Rev. Pharmacol. Toxicol., 23: 239–257.

Gilman, S.C., Bonner, M.J. and Pellmar, T.C. (1992) Peroxide effects on [^{3}H]L-glutamate release by synaptosomes isolated from the cerebral cortex, Neurosci. Lett., 140: 157–160.

Gilman, S.C., Bonner, M.J. and Pellmar, T.C. (1994) Free radicals enhance basal release of [^{3}H]D-aspartate from cerebral cortical synaptosomes, J. Neurochem., 62: 1757–1763.

Graf, E., Mahoney, J., Bryant, R. and Eaton, J. (1984) Iron-catalyzed hydroxyl radical formation a stringent requirement for free iron coordination site, J. Biol. Chem., 259: 3620–3624.

Griffith, O.W. and Meister, A. (1985) Origin and turnover of mitochondrial glutathione, Proc. Natl. Acad. Sci. USA, 82: 4668–4672.

Halliwell, B. (1977) Generation of hydrogen peroxide superoxide and hydroxyl radicals during the oxidation of dihydroxyfumaric acid by peroxidase, Biochem. J., 163: 441–448.

Halliwell, B. and Gutteridge, J.M.C. (1985) Oxygen radicals and the nervous system, Trends Neurosci., 8: 22–26.

Meister, A. (1983) Selective modification of glutathione metabolism, Science, 220: 472–477.

Mitchell, J.B. (1988) Glutathione modulation and cancer treatment, ISI Atlas of Science: Pharmacology, pp. 155–160.

Myers, L.S., Carmichael, A.J. and Pellmar, T.C. (1994) Radiation chemistry of the hippocampal brain slice, Adv. Space Res., 14: 453–(10)456.

Pellmar, T.C. (1986) Electrophysiological correlates of peroxide damage in guinea pig hippocampus in vitro, Brain Res., 364: 377–381.

Pellmar, T.C. (1987) Peroxide alters neuronal excitability in the CA1 region of guinea-pig hippocampus in vitro, Neuroscience, 23: 447–456.

Pellmar, T.C., Gilman, S.C., Keyser, D.O., Lee, K.J., Lepinski, D.L., Livengood, D. and Myers, L.S., Jr. (1994) Reactive oxygen species on neural transmission, Ann. New York Acad. Sci. USA, 738: 121–129.

Pellmar, T.C., Neel, K.L. and Lee, K.J. (1989) Free radicals mediate peroxidative damage in guinea pig hippocampus in vitro, J. Neurosci. Res., 24: 437–444.

Pellmar, T.C., Schauer, D.A. and Zeman, G.H. (1990) Time- and dose-dependent changes in neuronal activity produced by X-radiation in brain slices, Radiat. Res., 122: 209–214.

Pellmar, T.C., Hollinden, G.E. and Sarvey, J.M. (1991) Free radicals accelerate the decay of long-term potentiation in field CA1 of guinea pig hippocampus, Neuroscience, 44: 353–359.

Pellmar, T.C., Roney, D. and Lepinski, D.L. (1992) Role of glutathione in repair of free radical damage in hippocampus in vitro, Brain Res., 583: 194–200.

Pellmar, T.C. and Lepinski, D.L. (1992) Electrophysiological consequences of exposure of hippocampal slices to dihydroxyfumarate, a generator of superoxide radicals, Brain Res., 569: 189–198.

Pellmar, T.C. and Neel, K.L. (1989) Oxidative damage in the guinea pig hippocampal slice, Free Radical Biol. Med., 6: 467–472.

Raleigh, J.A., Kremers, W. and Gaboury, B. (1977) Dose-rate and oxygen effects in models of lipid membranes: linoleic acid, Int. J. Radiat. Biol. Relat. Stud. Phys. Chem. Med., 31: 203–213.

Reed, D.J. (1990) Review of the current status of calcium and thiols in cellular injury, Chem. Res. Toxicol., 3: 495–502.

Schauer, D.A., Zeman, G.H. and Pellmar, T.C. (1989) A low-energy X-ray irradiator for electrophysiological studies, Int. J. Rad. Appl. Instrum. A., 40: 7–17.

Schechter, Y., Burstein, Y. and Patchornik, A. (1975) Selective oxidation of methionine residues in proteins, Biochemistry, 14: 4497–4503.

Tolliver, J.M. and Pellmar, T.C. (1987) Ionizing radiation alters neuronal excitability in hippocampal slices of the guinea pig, Radiat. Res., 112: 555–563.

Volterra, A., Trotti, D., Tromba, C., Floridi, S. and Racagni, G. (1994) Glutamate uptake inhibition by oxygen free radicals in rat cortical astrocytes, J. Neurosci., 14: 2924–2932.

2314–2319 *Nucleic Acids Research, 1995, Vol. 23, No. 12*

Stereochemistry-dependent bending in oligonucleotide duplexes induced by site-specific covalent benzo[a]pyrene diol epoxide-guanine lesions

Rong Xu, Bing Mao+, Jing Xu, Bin Li, Sheryl Birke, Charles E. Swenberg[1] and Nicholas E. Geacintov*

Chemistry Department, 31 Washington Place, New York University, New York, NY 10003, USA and [1]Radiation Biochemistry Department, Armed Forces Radiobiology Research Institute, Bethesda, MD 20814, USA

Received December 21, 1994; Revised and Accepted May 2, 1995

ABSTRACT

The apparent persistence length of enzymatically linearized pIBI30 plasmid DNA molecules ~2300 bp long, as measured by a hydrodynamic linear flow dichroism method, is markedly decreased after covalent binding of the highly tumorigenic benzo[a]pyrene metabolite *7R,8S*-dihydroxy-*9S,10R*-epoxy-7,8,9,10-tetrahydrobenzo[a]pyrene [(+)-*anti*-BPDE]. In striking contrast, the binding of the non-tumorigenic, mirror-image *7S,8R,9R,10S* enantiomer [(–)-*anti*-BPDE] to DNA has no measurable effect on its alignment in hydrodynamic flow gradients (≤2.2% of the DNA bases modified). In order to relate this effect to BPDE-nucleotide lesions of defined stereochemistry, the bending induced by site-specifically placed and stereochemically defined (+)- and (–)-*anti*-BPDE-N^2-dG lesions in an 11mer deoxyoligonucleotide duplex was studied by ligation and gel electrophoresis methods. Out of the four stereochemically isomeric *anti*-BPDE-N^2-deoxyguanosyl (dG) adducts with either (+)-*trans*, (–)-*trans*, (+)-*cis*, and (–)-*cis* adduct stereochemistry, only the (+)-*trans* adduct gives rise to prominent bends or flexible hinge joints in the modified oligonucleotide duplexes. Since both *anti*-BPDE enantiomers are known to bind preferentially to dG (≥85%), these observations can account for the differences in persistence lengths of DNA modified with either (+)-*anti*-BPDE or the chiral (–)-*anti*-BPDE isomer.

INTRODUCTION

Polycyclic aromatic hydrocarbons, e.g. benzo[a]pyrene (BP), are metabolized *in vivo* to potent genotoxic diol epoxide derivatives that covalently bind to DNA (1–3). The resulting distortions in the native DNA conformation are believed to adversely affect the cellular processing of the modified DNA, and play an important role in mutagenesis (4,5), as well as in the initiation stages of tumorigenesis (6). The most tumorigenic metabolite of BP is the stereoisomer *7R,8S*-dihydroxy-*9S,10R*-epoxy-7,8,9,10-tetrahydrobenzo[a]pyrene [(+)-*anti*-BPDE]; interestingly, the mirror image *7S,8R,9R,10S* enantiomer [(–)-*anti*-BPDE] is not tumorigenic (7,8). The mutagenic activities of these two enantiomers are also strikingly different, the (+)-isomer being more mutagenic in mammalian cells, while the (–)-enantiomer is more active in bacterial cells (9–11). The molecular and structural origins of the differences in biological activities of (+)- and (–)-*anti*-BPDE have long been of interest (12,13). Both enantiomers react predominantly by opening of the epoxide ring at the C10 position of BPDE and by either *trans* or *cis* addition of the exocyclic amino group of guanine residues in DNA (14,15); the stereochemical properties of the four possible BPDE-N^2-dG lesions are depicted in Figure 1. The availability of site-specifically modified oligonucleotides with stereochemically different BPDE-N^2-dG lesions, has made possible a number of conformational (16–18), spectroscopic (19), thermodynamic (20,21), biochemical (22) and site-directed mutagenesis studies *in vitro* (23–25) and *in vivo* (26).

Structural alterations, such as the induction of bends or hinge joints at the sites of the lesions, may constitute significant forms of DNA damage (27,28). These structural distortions may affect recognition of the damaged DNA by repair enzymes, and adversely influence replication and transcription. Using transient electric linear dichroism and gel electrophoresis methods, Hogan *et al.* (29) demonstrated that the covalent binding of racemic *anti*-BPDE to 145–185 bp DNA fragments induces bends or kinks. The covalent binding of the (+)-*anti*-BPDE enantiomer to native DNA reduces its apparent persistence length, as measured by hydrodynamic flow linear dichroism techniques (30,31). While BPDE–deoxyguanine adducts are dominant, the BPDE–DNA adduct distribution is heterogeneous (15) and the loss in persistence length (30,31) cannot be directly associated with any of the stereochemically distinct guanine adduct forms (Fig. 1). In order to assess the effects of stereochemically different *anti*-BPDE-N^2-dG lesions on bending, we synthesized BPDE-modified deoxyoligonucleotides with site-specifically placed BPDE-N^2-dG lesions of defined stereochemistry. Using ligation

* To whom correspondence should be addressed

+Present address: Cellular and Biophysics Program, Memorial Sloan-Kettering Cancer Center, 1275 York Avenue, New York, NY 10021, USA

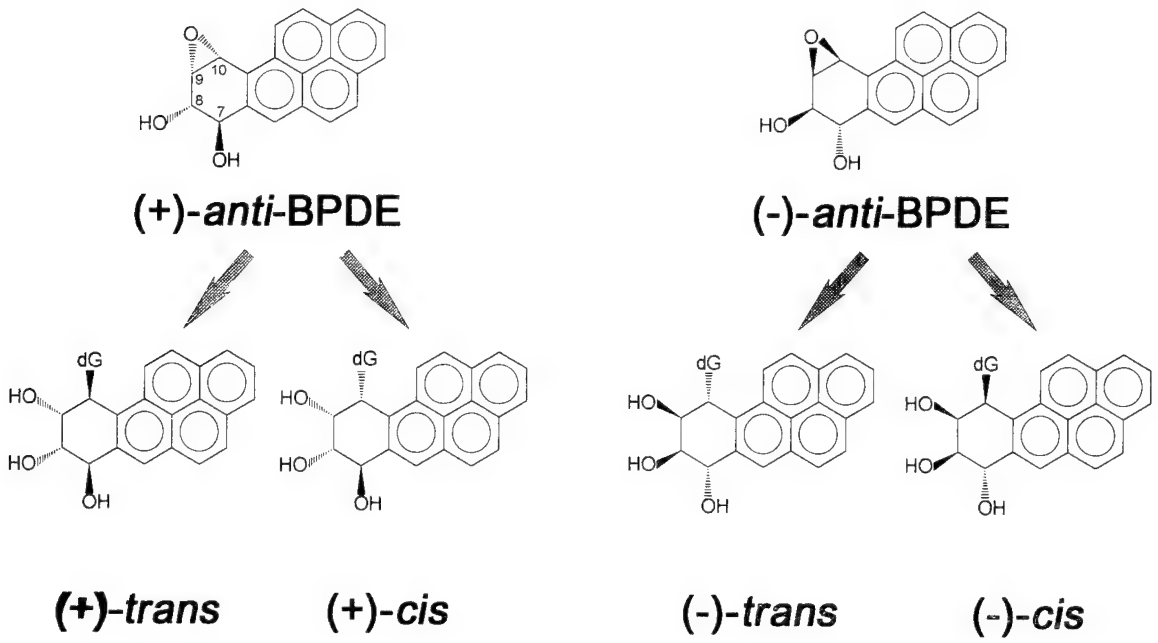

Figure 1. Stereochemistry of adducts resulting from the *trans*- or *cis*-addition of the two BPDE enantiomers to the exocyclic amino group of deoxyguanosine residues (dG).

and polyacrylamide gel electrophoresis methods, the electrophoretic mobilities of four stereochemically distinct isomeric BPDE-modified oligonucleotide duplexes were compared to one another.

MATERIALS AND METHODS

Preparation of BPDE-modified oligonucleotides

The oligonucleotides 5′-d(CACATGTACAC) and the strand 5′-d(GGTGTACATGT) were prepared by the phosphoramidite method using an automated DNA synthesizer. The (+)- and (–)-*anti*-BPDE enantiomers were purchased from the National Cancer Institute Chemical Carcinogen Reference Standard Repository (Chemsyn Sciences, Inc., Lot numbers 90-253-14-33 and 89-236-14-07, respectively). The stereochemically defined BPDE-modified oligonucleotides 5′-d(CACAT(G^{BPDE})TACAC), with (G^{BPDE}) = (+)-*trans-anti*-BPDE-N^2-dG, (–)-*trans-anti*-BPDE-N^2-dG, (+)-*cis-anti*-BPDE-N^2-dG, or (–)-*cis-anti*-BPDE-N^2-dG, were prepared by direct synthesis methods (32). Their stereochemical characteristics were ascertained as described previously for this particular sequence (19).

Labeling, ligation and gel electrophoresis

About 2 µg of each unmodified and BPDE-modified oligonucleotide were 5′-end-labeled with [γ-^{32}P]ATP (New England Nuclear) using 6 U of T4 polynucleotide kinase (Gibco Biological Research Laboratories) as described previously (22). After labeling with [γ-^{32}P]ATP, 2 µl of 0.1 M cold ATP (Pharmacia) and an additional 6 U of T4 polynucleotide kinase were added, and the reaction was continued at 37°C for an additional hour. The labeled unmodified and BPDE-modified single-stranded oligonucleotides were repurified using denaturing 20% polyacrylamide gel electrophoresis (7 M urea). The end-labeled and purified oligonucleotides were mixed with complementary strands designed to produce cohesive single-stranded ends, heated at 70°C for 10 min, and allowed to cool slowly to 8°C overnight, thus forming duplexes. The basic procedure of Koo *et al.* (33), with minor modifications, was used for ligating the following oligonucleotide duplexes (complementary: modified strand ratio 1.3:1) with cohesive ends at each end:

```
5′-CACATG*TACAC
   TGTAC ATGTGG-5′
```

Briefly, ~0.5 µg of these double-stranded oligonucleotides were incubated in 50 µl of ligation buffer solution (25 mM Tris–HCl, 5 mM $MgCl_2$, 0.5 mM ATP and 0.5 mM dithiothreitol, pH 7.6) and 10 U of T4 ligase (Gibco Biological Research Laboratories) at 12°C for ≥24 h. The ligated multimers were subjected to electrophoresis on non-denaturing 8% polyacrylamide gels in 0.1 M Tris-borate (pH 8.3), 2.5 mM EDTA (TBE buffer) at 4°C. The relative intensities of each of the bands were analyzed using a BIORAD 250 imaging system (Biorad, Hercules, CA).

BPDE-modified native DNA and flow linear dichroism measurements

The 2926 bp *Eco*RI enzyme restriction fragments of the plasmid pIBI30 were prepared as described previously (34), and were used in the hydrodynamic flow linear dichroism experiments because of their defined and homogeneous size. The DNA was reacted with either (+)- or (–)-*anti*-BPDE to generate BPDE-modified DNA molecules as described earlier (35). Aqueous DNA solutions were subjected to a hydrodynamic flow gradient in a Couette cell, and the absorbance was measured with linearly polarized light as described in detail elsewhere (34,35). The linear dichroism signal (LD) is defined as $A_{//} - A_{\perp}$, where $A_{//}$ and $A_{\perp}$ are the absorbances corresponding to the light polarization being oriented parallel or perpendicular to the flow direction, respectively

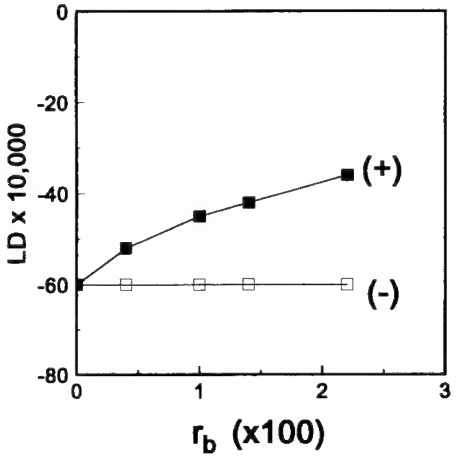

Figure 2. Linear dichroism signal measured at 260 nm of linearized pIBI30 fragments 2926 bp long covalently modified with (+)-BPDE (black squares) and (–)-BPDE (open squares) as a function of r_b, the fraction of modified bases. DNA concentration: 3.7×10^{-5} M (nucleotide concentration), in 5 mM Tris buffer solution (pH 7.9), 24 ± 1 °C. Flow gradient: 1800 s^{-1}. Additional details concerning the apparatus and methods of measurement are as previously described (34).

(36). The linear dichroism signal is proportional to the degree of alignment of the DNA molecules in the hydrodynamic flow gradient, and thus to the DNA persistence length (36).

RESULTS

Flow linear dichroism characteristics

The magnitude of the LD signal measured within the DNA absorption band at 260 nm is dominated by the DNA transition moments and thus reflects the degree of alignment of the DNA molecules. The DNA bases tend to align themselves with their planes perpendicular to the flow direction in the Couette cell, and the sign of the LD signal is thus negative at 260 nm (36).

The covalent binding of (+)-*anti*-BPDE causes increasingly large decreases in the magnitude of the LD signal with increasing r_b (number of BPDE residues/nucleotide) in the measured range of $r_b = 0.004–0.022$ (Fig. 2). These levels of binding correspond to one lesion per 25–125 bp, which are comparable with the average persistence length of unmodified native DNA [120–150 bp (37)]. In contrast to the effects caused by the (+)-stereoisomer, no observable changes in the hydrodynamic alignment of the (–)-*anti*-BPDE-modified DNA molecules up to $r_b = 0.022$ are observed (Fig. 2). Flow linear dichroism studies of (–)-*anti*-BPDE-modified calf thymus DNA were previously carried out only at low values of $r_b \leq 0.0037$), and the associated decrease in the LD signal was reported to be small (30). Our results span a wider range of r_b, and suggest that the adducts formed from (–)-*anti*-BPDE, unlike those derived from (+)-*anti*-BPDE, do not significantly perturb the overall persistence length of DNA. Although guanine residues are the major targets of binding of *anti*-BPDE in DNA, the adduct distribution is heterogeneous (15) and the bending effects cannot be directly and unambiguously associated with a particular lesion. However, the bending induced by stereochemically distinct *anti*-BPDE-N^2-dG lesions, can be examined by ligating site-specifically modified oligonucleotide duplexes, and by examining the electrophoretic mobilities of the ligation products on native polyacrylamide gels.

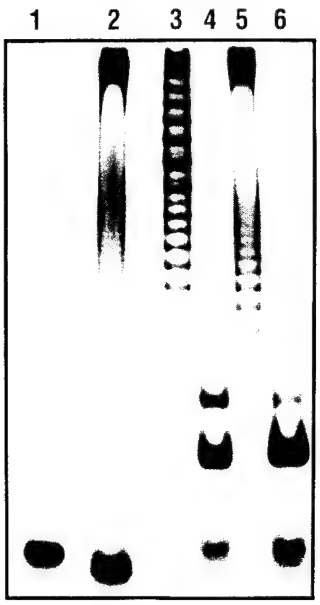

Figure 3. Ligation ladders of unmodified 11mer duplexes 5′-d(CACATGTACAC)•5′-d(GGTGTACATGT) (lane 2), and BPDE-modified duplexes 5′-d(CACAT(G^{BPDE})TACAC)•5′-d(GGTGTACATGT) with (+)-*trans*- (lane 3), (+)-*cis*- (lane 4), (–)-*trans*- (lane 5), and (–)-*cis*-adduct stereochemistry (lane 6). The single band in lane 1 is due to an unligated standard 11mer duplex used as a size marker (see text).

Gel electrophoresis of self-ligated oligonucleotides

A typical autoradiograph of a non-denaturing electrophoresis gel of ligation products of the BPDE-modified and unmodified 11mers is shown in Figure 3. Lane 1 represents the electrophoretic migration of an unmodified 11mer duplex 5′-d(CCATCGCTACC)•5′-d(GGGTAGCGATG) that is routinely used as a standard size-marker in our laboratory. Lane 2 represents the migration of a mixture of multimers of the ligated unmodified 11mer duplex 5′-d(CACATGTACAC)•d(GGTGTACATGT); lanes 3, 4, 5 and 6 represent electrophoretic mobility patterns of the ligation mixtures of the BPDE-modified duplexes 5′-d(CACAT(G^{BPDE})TACAC)•5′-d(GGTGTACATGT), with (G^{BPDE}) representing the (+)-*trans*- (lane 3), (+)-*cis*- (lane 4), (–)-*trans*- (lane 5), and (–)-*cis*-*anti*-BPDE-N^2-dG lesions (lane 6). In general, the appearance of these kinds of gels are variable, and depend not only on the ligation reaction time and the amount of enzyme, but also on the exposure time. The exposure of the photograph in Figure 3 was adjusted so as to emphasize the unusual set of dark bands in the upper portion of lane 3; some of the fainter, higher mobility bands are therefore poorly visible in this photograph. However, these fainter bands are evident in the densitometer tracings of lanes 2, 3 and 5 for the unmodified, (+)-*trans*-, and (–)-*trans*-BPDE-modified oligonucleotide duplexes (Fig. 4). Similar densitometer tracings were obtained with the (–)-*cis*- and (+)-*cis* oligomer adducts (lanes 4 and 6) that revealed a total of four and five variable-intensity bands, respectively (data not shown).

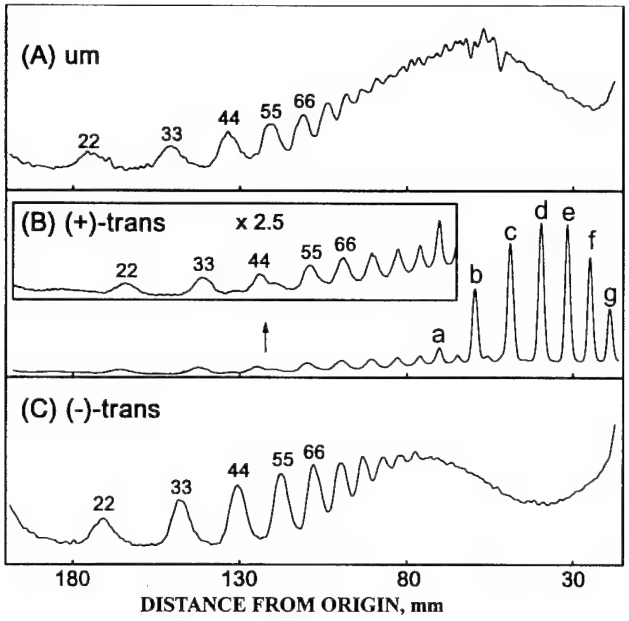

Figure 4. Densitometer tracings of lanes 2, 3 and 5 in Figure 3. (**A**) Unmodified (um) multimer duplexes (from lane 2 in Fig. 3). (**B**) (+)-*trans*-multimer adduct duplexes (from lane 3 in Fig. 3); the lower molecular weight portion corresponding to the normal progression of multimers is shown in the box at a 2.5× magnification. (**C**) (–)-*trans*-multimer adduct duplexes (from lane 5 in Fig. 3). The numbers above the bands denote the sequence lengths in base pairs. The circular DNA molecules are labeled 'a'–'g' (see text).

Remarkable adduct stereochemistry-dependent differences in the products of the ligation reactions are observed. These differences are summarized below.

Differences in [γ-^{32}P]ATP end-labeling and ligation efficiencies

A difference in [γ-^{32}P]ATP end-labeling efficiencies was noted during the course of these experiments. The efficiencies of labeling of *trans* and *cis* oligonucleotide adducts were about 40–50% and 70–80% as efficient, respectively, as the efficiency of labeling the unmodified 11mers. Thus, the amounts of labeled 11mers recovered in the five different samples (Fig. 3) were not entirely identical. Since identical amounts of complementary strands were added in each case, the actual ratio of complementary:labeled strands was highest in the case of the two *trans* adducts, and lowest in the case of the unmodified adducts. An excess of unligated 11mers is particularly pronounced at the bottom of lane 2 (Fig. 3); a closer analysis showed that these bands are mixtures of single-stranded and double-stranded unmodified 11mers (data not shown). The variable amounts of unligated 11mers in lanes 2, 4 and 6 (Fig. 3) are thus attributed, at least in part, to differences in the amount of labeled BPDE-modified strands recovered in the end-labeling experiments; this can lead to an insufficient excess of complementary strands, thus leading to partial dissociation of the duplexes, and inefficient ligation reactions.

High molecular weight ligation products are observed in all cases except in the cases of the two *cis* adducts (Fig. 3). In the case of the (+)-*trans*-BPDE adducts, much of the high molecular weight material is concentrated in six closely spaced intense bands at the top of lane 3 in Figure 3. There is a noticeable lack of higher molecular weight (+)-*cis*- and (–)-*cis*-multimer adducts (lanes 4 and 6 in Fig. 3). The ligation efficiencies of the (+)-*cis*- and (–)-*cis*-adduct duplexes are thus clearly lower than those of the unmodified and (+)-*trans*- and (–)-*trans*-adduct duplexes (lanes 4 and 5). The amount of *cis*-22mers is higher than the amount of 11mer or 33mers (lanes 4 and 6). These differences are greater than might be expected on the basis of a series of consecutive ligation reactions, each with similar rate constants. However, we noticed that the activity of the ligase decreases steadily during the course of the reactions; thus, quantitative comparisons of the amounts of different multimers formed is difficult, particularly with the slowly ligating *cis*-oligonucleotide adducts, and the origins of these effects were not further pursued. The differences in ligation efficiencies of the pairs of *trans* and *cis* oligonucleotide adducts may be associated with differences in adduct conformations. The *trans* adducts are characterized by external adduct conformations, while the *cis* adducts are intercalative in nature (19), as has been established for BPDE-N^2-dG in a similar sequence by high resolution NMR (16–18) and low resolution optical spectroscopic methods (21).

Electrophoretic mobilities

All of the oligonucleotide multimers containing BPDE residues migrate more slowly than the unmodified oligonucleotide multimers with the same number of base pairs, and thus are characterized by longer apparent sequence lengths. The slower mobilities of the BPDE-modified duplexes and their multimers as compared to the unmodified oligomers can be attributed, at least in part, to the additional mass of the BPDE residue. An examination of the densitometry traces (e.g. Fig. 4, and data not shown) indicate that the electrophoretic mobilities are arranged in the following order: unmodified > (–)-*trans* > (+)-*cis* $\gtrsim$ (–)-*cis* > (+)-*trans* oligomers. The unusual relatively slow mobility of the (+)-*trans*-oligonucleotide adducts is revealed even more strikingly in plots of R_L versus the number of base pairs in each multimer (Fig. 5), where (33)

$$R_L = (\text{apparent length})/(\text{sequence length})$$

The apparent lengths of the BPDE-modified multimers are obtained by extrapolation of migration distances of a given BPDE-modified multimer band situated between two unmodified multimer bands of known sequence length. The migration distances are most easily evaluated from the densitometer tracings (e.g., Fig. 4).

The value of R_L is significantly greater, and its value increases more strongly as a function of increasing sequence length in the case of the (+)-*trans* adducts (Fig. 5). The larger R_L ratios are indicative of a greater degree of bending or of more prominent flexible hinge joints in (+)-*trans*-BPDE-modified duplexes than in the (–)-*trans*-, (+)-*cis*- and (–)-*cis*-BPDE-modified duplexes. The degree of bending associated with the multimers bearing the stereoisomeric (–)-*trans*-BPDE-N^2-dG lesions is apparently not sufficient to observe ring-closure, and minicircles are thus not observed in lane 4. From the data in Figure 3, no conclusions regarding minicircle formation can be reached in the case of the

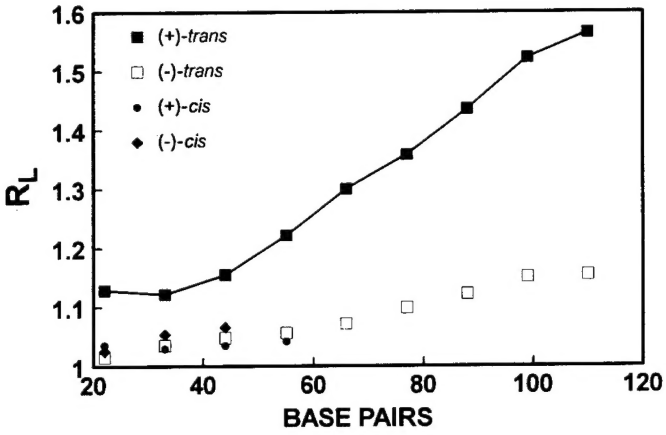

Figure 5. Plot of R_L-ratio as a function of sequence length, expressed in terms of the number of base pairs per DNA molecule.

two *cis* adducts, since the extent of ligation of the two *cis* adducts is insufficient.

Minicircle formation upon ligation of (+)-*trans* adducts

Much of the radioactivity is concentrated in the six prominent bands visible in the upper portion of lane 3 in Figure 3 (panel B in Fig. 4). Employing two-dimensional gel electrophoresis techniques (38,39), Mao has shown that these types of intense bands, which are observed only when (+)-*trans*-BPDE-modified oligonucleotide duplexes are ligated, are minicircles (40). Ring closure upon ligation is facilitated by bends and/or the flexibilities of the DNA molecules (41), and is thus a useful tool for studying the flexibilities and persistence lengths of DNA duplexes (42). Ongoing work on the characterization of these minicircles by known methods (38,39) shows that the size of the smallest minicircle is 77 bp (labeled 'a' in Fig. 4B), and that the six larger ones ('b'–'g') vary in size from 88 to 143 bp (Xu, R., Mao, B., Amin, S. and Geacintov, N.E., in preparation).

DISCUSSION

Correlation of reduced electrophoretic mobilities with alterations in hydrodynamic alignment of BPDE-modified native DNA fragments

When native DNA is reacted with either (+)-*anti*-BPDE or (–)-*anti*-BPDE, all four stereochemically possible adducts are formed in different proportions. In the case of the (+)-enantiomer, 94% are (+)-*trans*-BPDE-N^2-dG, 3% (+)-*cis*-adducts and 1% or less of the adducts involve binding to adenine residues. The adduct distribution generated by the (–)-*anti*-BPDE isomer is 58% (–)-*trans*-BPDE-dG, 5% (–)-*cis*-BPDE-N^2-dG and 15% (+)-*trans*-BPDE-N^6-dA adducts (15). The (+)-*trans*-BPDE-N^2-dG lesions outnumber all of the others by a factor of 20:1; thus, it may be assumed that the reduced alignment of (+)-*anti*-BPDE-modified DNA in hydrodynamic flow gradients (30,31) or transient electric fields (29), is associated with the dominant (+)-*trans*-BPDE-N^2-dG lesions.

Since the flow linear dichroism characteristics of (–)-*anti*-BPDE-modified DNA are not measurably affected in the same range of r_b (Fig. 2), we conclude that neither the (–)-*trans*- or (–)-*cis*-BPDE-N^2-dG, nor the (+)-*trans*-BPDE-N^6-dA lesions, significantly alter the persistence length of the modified DNA. The gel electrophoresis data is consistent with this conclusion since only oligonucleotide duplexes with (+)-*trans*-BPDE-N^2-dG lesions exhibit markedly slower electrophoretic mobilities than those containing any of the other three modified guanines. The gel electrophoresis studies presented here were obtained in a single sequence context. It will be of great interest to investigate the effects of base sequence on the nature of the bends (flexible versus static, degree of bending, etc.). Such investigations, especially the effects of bases flanking the modified Gs on circle size, are presently underway in our laboratory.

Finally, we note that structural distortions such as bends and flexible hinge joints induced by the covalent binding of drugs or bulky mutagenic and/or carcinogenic compounds are not uncommon. Examples of such ligands include 2-aminofluorene and its *N*-2-acetyl-derivative (27), (+)-CC1065 (43), cis-platin adducts (44), UV light-induced thymine dimers (45) and certain positional and configurational isomers of the polycyclic aromatic diol epoxide derivatives of 5-methylchrysene (34) and benz[a] anthracene (46).

ACKNOWLEDGEMENTS

This work was supported by the Office of Health and Environmental Research, the Department of Energy (DE-FGO2-86ER-60405). The synthesis of the BPDE-modified oligonucleotides was supported by Grant CA 20851 from the National Cancer Institute, National Institutes of Health.

REFERENCES

1 Singer, B. and Grunberger, D. (1983) *Molecular Biology of Mutagens and Carcinogens*, Plenum Press, NY.
2 Harvey, R.G., *Polycyclic Aromatic Hydrocarbons: Chemistry and Carcinogenicity*, Cambridge University Press, 1991.
3 Conney, A.H. (1982) *Cancer Res.* **42**, 4875–4917.
4 Rodriguez, H. and Loechler, E.L. (1993) *Carcinogenesis* **14**, 373–383.
5 Rodriguez, H. and Loechler, E.L. (1993) *Biochemistry* **32**, 1759–1769 (1993).
6 Harris, C.C. (1991) *Cancer Res. (Suppl.)* **51**, 5023s–5044s.
7 Buening, M.K., Wislocki, P.G., Levin, W., Yagi, H., Thakker, D.R., Akagi, H., Koreeda, M., Jerina, D.M. and Conney, A.H. (1978) *Proc. Natl. Acad. Sci. USA* **75**, 5358–5361.
8 Slaga, T.J., Bracken, W.J., Gleason, G., Levin, W., Yagi, H., Jerina, D.M. and Conney, A.H. (1979) *Cancer Res.* **39**, 67–71.
9 Wood, A.W., Chang, R.L., Levin, W., Yagi, H., Thakker, D.R., Jerina, D.M. and Conney, A.H. (1977) *Biochem. Biophys. Res. Commun.* **77**, 1389–1396.
10 Stevens, C.W., Bouck, N., Burgess, J.A. and Fahl, W.E. (1985) *Mutation Res.* **152**, 5–14.
11 Brookes, P. and Osborne, M.R. (1982) *Carcinogenesis* **3**, 1223–1226.
12 Geacintov, N.E. (1988) In Yang, S.K. and Silverman, B.D. (eds) *Polycyclic Aromatic Hydrocarbon Carcinogenesis: Structure–Activity Relationships.* CRC Press, Boca Raton, FL, Vol. II, pp. 181–206.
13 Gräslund, A. and Jernström, B. (1989) *Q. Rev. Biophys.* **22**, 1–37.
14 Meehan, T. and Straub, K. (1979) *Nature* **277**, 410–412.
15 Cheng, S.C., Hilton, B.D., Roman, J.M. and Dipple, A. (1989) *Chem. Res. Toxicol.* **2**, 334–340.
16 Cosman, M., de los Santos, C., Fiala, R., Hingerty, B.E., Ibanez, V., Margulis, L.A., Live, D., Geacintov, N.E., Broyde, S. and Patel, D.J. (1992) *Proc. Natl. Acad. Sci. USA* **89**, 1914–1918.
17 de los Santos, Cosman, M., Hingerty, B.E., Ibanez, V., Margulis, L.A., Geacintov, N.E., Broyde, S. and Patel, D.J. (1992) *Biochemistry* **31**, 5245–5252.
18 Cosman, M., de los Santos, C., Fiala, R., Hingerty, B.E., Ibanez, V., Luna, E., Harvey, R.G., Geacintov, N.E., Broyde, S. and Patel, D. (1993) *Biochemistry* **32**, 4145–4155.

19 Geacintov, N.E., Cosman, M., Mao, B., Alfano, A., Ibanez, V. and Harvey, R.G. (1991) *Carcinogenesis* **12**, 2099–2108.
20 Cosman, M., Geacintov, N.E. and Amin, S. (1993). In Garrigues, P. and Lamotte, M. (eds) *Polycyclic Aromatic Compounds. Synthesis, Properties, Analytical Measurements, Occurrence and Biological Effects.* Gordon & Breach, Switzerland, pp. 1151–1158.
21 Ya, N.-Q., Smirnov, S., Cosman, M., Bhanot, S., Ibanez, V. and Geacintov, N.E. (1994) In R.H. Sarma and M.H. Sarma (eds) *Structural Biology: The State of the Art. Proceedings of the 8th Converstaion.* Adenine Press, Schenectady, NY, Vol. 2, pp. 349–366 (1994).
22 Mao, B., Li, B., Amin, S., Cosman, M. and Geacintov, N.E. (1993) *Biochemistry* **32**, 11785–11793.
23 Hruszkewycz, A.M., Canella, K.A., Peltonen, K., Kotrappa, L. and Dipple, A. (1992) *Carcinogenesis* **13**, 2347–2352.
24 Shibutani, S., Margulis, L.A., Geacintov, N.E. and Grollman, A.P. (1993) *Biochemistry* **32**, 7531–7541.
25 Choi, D.-J., Marino-Alessandri, D.J., Geacintov, N.E. and Scicchitano, D.A. (1994) *Biochemistry* **33**, 780–787.
26 Mackay, W., Benasutti, M., Drouin, E. and Loechler, E.L. (1992) *Carcinogenesis* **13**, 1415–1425.
27 Schwartz, A., Marrot, L. and Leng, M. (1989) *J. Mol. Biol.* **207**, 445–450.
28 Leng, M. (1990) *Biophys. Chem.* **35**, 155–163.
29 Hogan, M.E., Dattagupta, N. and Whitlock, J.P., Jr (1981) *J. Biol. Chem.* **256**, 4504–4513.
30 Eriksson, M., Nordén, B., Jernström, B. and Gräslund, A. (1988) *Biochemistry* **27**, 1213–1221.
31 Roche, C.J. Geacintov, N.E., Ibanez, V. and Harvey, R.G. (1989) *Biophys. Chem.* **33**, 277–288.
32 Cosman, M., Ibanez, V., Geacintov, N.E. and Harvey, R.G. (1990) *Carcinogenesis* **11**, 1667–1672.
33 Koo, H.-S., Wu, H.-M. and Crothers, D.M. (1986) *Nature* **320**, 501–506.
34 Balasta, L., Xu, R., Geacintov, N.E., Swenberg, C.E., Amin, S. and Hecht, S.S. (1993) *Chem. Res. Toxicol.* **6**, 616–624.
35 Xu, R., Birke, S., Carberry, S.E., Geacintov, N.E., Swenberg, N.E. and Harvey, R.G. (1992) *Nucleic Acids Res.* **20**, 6167–6176.
36 Norden, B., Kubista, M. and Kurucsev, T. (1992) *Q. Rev. Biophys.* **25**, 51–170.
37 Hagerman, P.J. (1988) *Annu. Rev. Biophys. Biophys. Chem.* **17**, 265–286.
38 Zahn, K. and Blattner, F.R. (1987) *Science* **236**, 416–422.
39 Ulanovsky, L., Bodner, M., Trifonov, E.N. and Choder, M. (1986) *Proc. Natl. Acad. Sci. USA* **83**, 862–866.
40 Mao, B. (1993) Ph.D. Dissertation, New York University.
41 Shore, D., Langowski, J. and Baldwin, R.L. (1981) *Proc. Natl. Acad. Sci. USA* **78**, 4833–4837.
42 Hagerman, P.J. and Ramadevi, V.A. (1990) *J. Mol. Biol.* **212**, 351–362.
43 Lin, C.H., Sun, D. and Hurley, L.H. (1991) *Chem. Res. Toxicol.* **4**, 21–26.
44 Bellon, S.F. and Lippard, S.J. (1990) *Biophys. Chem.* **35**, 179–188.
45 Wang, C.-I. and Taylor, J.S. (1991) *Proc. Natl. Acad. Sci.USA* **88**, 9072–9076.
46 Carberry, S.E., Geacintov, N.E. and R.G. Harvey (1989) *Carcinogenesis* **10**, 97–103.

DISTRIBUTION LIST

DEPARTMENT OF DEFENSE

ARMED FORCES RADIOBIOLOGY RESEARCH INSTITUTE
ATTN: PUBLICATIONS BRANCH
ATTN: LIBRARY

ARMY/AIR FORCE JOINT MEDICAL LIBRARY
ATTN: DASG-AAFJML

ASSISTANT TO THE SECRETARY OF DEFENSE
ATTN: AE
ATTN: HA(IA)

DEFENSE NUCLEAR AGENCY
ATTN: TITL
ATTN: DDIR
ATTN: RAEM
ATTN: MID

DEFENSE TECHNICAL INFORMATION CENTER
ATTN: ACQUISITION
ATTN: ADMINISTRATOR

FIELD COMMAND DEFENSE NUCLEAR AGENCY
ATTN: FCIEO

INTERSERVICE NUCLEAR WEAPONS SCHOOL
ATTN: DIRECTOR

LAWRENCE LIVERMORE NATIONAL LABORATORY
ATTN: LIBRARY

UNDER SECRETARY OF DEFENSE (ACQUISITION)
ATTN: OUSD(A)/R&E

UNIFORMED SERVICES UNIVERSITY OF THE HEALTH SCIENCES
ATTN: LIBRARY

DEPARTMENT OF THE ARMY

HARRY DIAMOND LABORATORIES
ATTN: SLCSM-SE

OFFICE OF THE SURGEON GENERAL
ATTN: MEDDH-N

U.S. ARMY AEROMEDICAL RESEARCH LABORATORY
ATTN: SCIENCE SUPPORT CENTER

U.S. ARMY CHEMICAL RESEARCH, DEVELOPMENT, & ENGINEERING CENTER
ATTN: SMCCR-RST

U.S. ARMY INSTITUTE OF SURGICAL RESEARCH
ATTN: COMMANDER

U.S. ARMY MEDICAL DEPARTMENT CENTER AND SCHOOL
ATTN: MCCS-FCM

U.S. ARMY MEDICAL RESEARCH AND MATERIEL COMMAND
ATTN: COMMANDER

U.S. ARMY MEDICAL RESEARCH INSTITUTE OF CHEMICAL DEFENSE
ATTN: MCMR-UV-R

U.S. ARMY NUCLEAR AND CHEMICAL AGENCY
ATTN: MONA-NU

U.S. ARMY RESEARCH INSTITUTE OF ENVIRONMENTAL MEDICINE
ATTN: DIRECTOR OF RESEARCH

U.S. ARMY RESEARCH LABORATORY
ATTN: DIRECTOR

WALTER REED ARMY INSTITUTE OF RESEARCH
ATTN: DIVISION OF EXPERIMENTAL THERAPEUTICS

DEPARTMENT OF THE NAVY

BUREAU OF MEDICINE & SURGERY
ATTN: CHIEF

NAVAL AEROSPACE MEDICAL RESEARCH LABORATORY
ATTN: COMMANDING OFFICER

NAVAL MEDICAL RESEARCH AND DEVELOPMENT COMMAND
ATTN: CODE 42

NAVAL MEDICAL RESEARCH INSTITUTE
ATTN: LIBRARY

NAVAL RESEARCH LABORATORY
ATTN: LIBRARY

OFFICE OF NAVAL RESEARCH
ATTN: BIOLOGICAL & BIOMEDICAL S&T

DEPARTMENT OF THE AIR FORCE

BROOKS AIR FORCE BASE
ATTN: AL/OEBZ
ATTN: OEHL/RZ
ATTN: USAFSAM/RZB

OFFICE OF AEROSPACE STUDIES
ATTN: OAS/XRS

OFFICE OF THE SURGEON GENERAL
ATTN: HQ AFMOA/SGPT
ATTN: HQ USAF/SGES

U.S. AIR FORCE ACADEMY
ATTN: HQ USAFA/DFBL

U.S. AIR FORCE OFFICE OF SCIENTIFIC RESEARCH
ATTN: DIRECTOR OF CHEMISTRY & LIFE SCIENCES

OTHER FEDERAL GOVERNMENT

ARGONNE NATIONAL LABORATORY
ATTN: ACQUISITIONS

BROOKHAVEN NATIONAL LABORATORY
ATTN: RESEARCH LIBRARY, REPORTS SECTION

CENTER FOR DEVICES AND RADIOLOGICAL HEALTH
ATTN: DIRECTOR

GOVERNMENT PRINTING OFFICE
ATTN: DEPOSITORY ADMINISTRATION BRANCH
ATTN: CONSIGNED BRANCH

LIBRARY OF CONGRESS
ATTN: UNIT X

LOS ALAMOS NATIONAL LABORATORY
ATTN: REPORT LIBRARY

NATIONAL AERONAUTICS AND SPACE ADMINISTRATION
ATTN: RADLAB

NATIONAL AERONAUTICS AND SPACE ADMINISTRATION
GODDARD SPACE FLIGHT CENTER
ATTN: LIBRARY

NATIONAL CANCER INSTITUTE
ATTN: RADIATION RESEARCH PROGRAM

NATIONAL DEFENSE UNIVERSITY
ATTN: LIBRARY

NATIONAL INSTITUTE OF STANDARDS AND TECHNOLOGY
ATTN: IONIZING RADIATION DIVISION

U.S. DEPARTMENT OF ENERGY
ATTN: LIBRARY

U.S. FOOD AND DRUG ADMINISTRATION
ATTN: WINCHESTER ENGINEERING AND ANALYTICAL CENTER

U.S. NUCLEAR REGULATORY COMMISSION
ATTN: LIBRARY

RESEARCH AND OTHER ORGANIZATIONS

AUSTRALIAN DEFENCE FORCE
ATTN: SURGEON GENERAL

AUTRE, INC.
ATTN: PRESIDENT

BRITISH LIBRARY
ATTN: ACQUISITIONS UNIT

CENTRE DE RECHERCHES DU SERVICE DE SANTE DES ARMEES
ATTN: DIRECTOR

FEDERAL ARMED FORCES DEFENSE SCIENCE AGENCY FOR NBC PROTECTION
ATTN: LIBRARY

INHALATION TOXICOLOGY RESEARCH INSTITUTE
ATTN: LIBRARY

INSTITUTE OF RADIOBIOLOGY, ARMED FORCES MEDICAL ACADEMY
ATTN: DIRECTOR

KAMAN SCIENCES CORPORATION
ATTN: DASIAC

OAK RIDGE ASSOCIATED UNIVERSITIES
ATTN: MEDICAL LIBRARY

RESEARCH CENTER FOR SPACECRAFT RADIATION SAFETY
ATTN: DIRECTOR

RUTGERS UNIVERSITY
ATTN: LIBRARY OF SCIENCE AND MEDICINE

UNIVERSITY OF CALIFORNIA
ATTN: DIRECTOR, INSTITUTE OF TOXICOLOGY & ENVIRONMENTAL HEALTH
ATTN: LIBRARY, LAWRENCE BERKELEY LABORATORY

UNIVERSITY OF CINCINNATI
ATTN: UNIVERSITY HOSPITAL, RADIOISOTOPE LABORATORY

XAVIER UNIVERSITY OF LOUISIANA
ATTN: COLLEGE OF PHARMACY